GPS Solutions (2022) 26:71
https://doi.org/10.1007/s10291-022-01255-x

ORIGINAL ARTICLE

GNSS carrier phase time-variant observable-specific signal bias (OSB) handling: an absolute bias perspective in multi-frequency PPP

Ke Su[1,2] · **Shuanggen Jin**[3] · **Guoqiang Jiao**[1,2,3]

Received: 14 August 2021 / Accepted: 28 March 2022

Abstract

In precise satellite clock estimation, the satellite clock offsets absorb the pseudorange and carrier phase time-variant hardware delays. The dissimilarity of the satellite clock estimated with observations at different frequencies is termed the inter-frequency clock bias (IFCB). The bias inconsistency suggests that the simple ionospheric-free satellite clock cannot directly be applied to the multi-frequency carrier phase observations in multi-frequency precise point positioning (PPP). We propose the carrier phase time-variant observable-specific signal bias (OSB) concept and the corresponding estimation approach to solve this. The definition, rationality, reliability and validity of the carrier phase time-variant OSB are clarified. The new concept advantage is that a set of the carrier phase time-variant OSB values can directly amend on the carrier phase observations, and thereafter, the IFCB effect can be eliminated, which provides the flexibilities for the GNSS carrier phase observation handing. Datasets collected from 144 Multi-GNSS Experiment (MGEX) stations are adopted for the carrier phase time-variant OSB estimation and an analysis of its effect on the GNSS multi-frequency PPP performance. The various multi-frequency PPP models are tested and evaluated considering the carrier phase time-variant OSB correction. The results indicate that the GPS, BDS-2 and BDS-3 carrier phase time-variant OSB time series have the obvious amplitudes and the amplitudes of the Galileo and QZSS carrier phase time-variant OSB are small. The GPS and BDS-2 multi-frequency PPP performance is significantly enhanced when correcting the carrier phase time-variant OSB. The GPS-only kinematic ionospheric-float PPP exhibits the positioning accuracy of 1.0 cm, 2.2 cm and 2.6 cm in the north, east and up components when correcting the carrier phase time-variant OSB, whereas the positioning accuracy of the case without the correction is 1.4 cm, 2.8 cm and 3.7 cm in three directions, respectively. The mean convergence time of two dual-frequency and three triple-frequency BDS-2-only kinematic PPP is reduced by 5.0%, 4.9%, 5.4%, 4.7% and 4.6%, respectively, with the carrier phase time-variant OSB correction. The carrier phase time-variant OSB improvement on BDS-3-only multi-frequency PPP is not obvious owing to the relatively few available and stable carrier phase time-variant OSB values. The reliability, suitability and effectiveness of the GNSS carrier phase time-variant OSB are demonstrated.

Keywords Carrier phase time-variant OSB · Inter-frequency clock bias (IFCB) · Multi-frequency PPP · Positioning accuracy · Convergence time

Introduction

With the acceleration of Global Navigation Satellite System (GNSS) modernization, the observation signals have gradually developed from dual- to triple- and even more frequencies. The Global Positioning System (GPS) Block IIF satellites are capable of transmitting the L1, L2 and L5 signals. The regional Beidou Navigation Satellite System (BDS-2) satellites can broadcast the B1I, B2I and B3I signals. The global BDS (BDS-3) satellites can broadcast the B2b, B1C, B2a, B2(B2a + B2b) signals and the BDS-2 legacy B1I and B3I signals. Galileo satellites can provide the observations at the E1, E5a, E5b, E5 and

✉ Ke Su
suke17@mails.ucas.ac.cn

[1] University of Chinese Academy of Sciences, Beijing 100049, China

[2] Multi-GNSS Positioning and Analysis System R&D Center, Qingdao 266000, China

[3] Shanghai Astronomical Observatory, Chinese Academy of Sciences, Shanghai 200030, China

Published online: 22 April 2022

E6 frequencies. As to the Quasi-Zenith Satellite System (QZSS) satellites, the L1, L2, L5 and L6 signals can be observed. The multi-frequency observations have better prospects for cycle slip detection, precise positioning, rapid ambiguity resolution, ionospheric modeling and so on (Dvulit et al. 2021; Li et al. 2020b; Liu et al. 2020; Ma et al. 2021).

The pseudorange and carrier phase hardware delays need to be handled correctly and carefully in the multi-frequency PPP handling, largely relying on the signal modulation type and frequency. Generally, the precise satellite clock products are solved with the specific dual-frequency observations (e.g., GPS L1/L2 and BDS B1I/B3I signals) (Zhao et al. 2018). During the precise clock estimation (PCE), the satellite clock offsets will absorb the pseudorange and carrier phase time-variant hardware delays. Hence, the satellite clock offsets estimated with different measurements are inconsistent. The disagreement is termed the inter-frequency clock bias (IFCB), which contains the pseudorange and carrier phase part. The estimability of multi-frequency and multi-GNSS biases and clock has already been studied in plentiful publications (Khodabandeh and Teunissen 2016; Odijk et al. 2016; Zhang et al. 2017, 2019). One way to solve the IFCB issue is to estimate precise satellite clock products for all existing frequency bands. For instance, Guo and Geng (2018) proposed to provide the GPS L1/L2 and L5-only two types of satellite clock products for the triple-frequency precise point positioning (PPP), by which the GPS multi-frequency observations can be compatible with each other. However, the drawback is that the computational burden is too heavy, and it is difficult to provide all the specific-frequency clock products in precise positioning. Another substitutable solution is to apply the IFCB values. The potential multi-frequency signals are all compatible with the specific satellite clocks and corresponding IFCB values.

The pseudorange IFCB is affected by the elevation- and frequency- group delay variations at the antenna reception and transmission parts (Wanninger et al. 2017), and acts as the important error source in the GNSS precise positioning and ionospheric modeling, which are usually calibrated by the differential code bias (DCB) or pseudorange observable-specific signal bias (OSB) products (Wang et al. 2016). In the era of the multi-frequency GNSS signals, the pseudorange OSB is more popular and has advantages on usability for it can dramatically reduce the provided parameter number. The GNSS pseudorange OSB has been popularized, applied, and defined in the SINEX 1.00 format, which can be directly corrected in the GNSS raw code measurements (Schaer 2016; Wang et al. 2020). As to the carrier phase IFCB, Pan et al. (2017b) demonstrated that the GPS peak-to-peak IFCB amplitude is 0.023–0.269 m using the 129 Multi-GNSS Experiment (MGEX) stations for a whole year. The GPS carrier phase IFCB sub-daily variations have periodic properties and are related to the sun–spacecraft–earth geometry (Montenbruck et al. 2012a). Consequently, the GPS carrier phase IFCB can be predicted and modeled with high accuracy using the periodic empirical function (Li et al. 2016). The BDS-2 IFCB variations are small and generally have peak amplitudes of approximately 2–4 cm (Liu et al. 2020; Montenbruck et al. 2012a). As to other GNSS satellites, the Galileo, QZSS and the BDS-3 experimental satellites exhibit the great consistency of the multi-frequency signals (Cai et al. 2016; Hauschild et al. 2012; Pan et al. 2017a). The large amplitude of the IFCB will seriously degrade the positioning accuracy and must be considered in the precise positioning. Besides, the high-quality GNSS uncalibrated phase delay (UPD) estimate production needs the IFCB correction to effectively conduct the PPP ambiguity resolution (Li et al. 2020a). The epoch-differenced strategy can rapidly estimate the IFCB when eliminating the phase ambiguities by the between-epoch single-difference approach (Li et al. 2012; 2016; Pan et al. 2019). In the current environment of multi-GNSS, the further understanding of the GNSS IFCB, especially for newly BDS-3 IFCB, needs to be characterized. Moreover, the compatibility of the estimated IFCB for different combined measurements is also the focus of the issue. Pan et al. (2019) rigorously derived the mathematical relationships of GPS L5-only, L1/L5, and L1/L2/L5 ionospheric-free (IF) IFCB, showing that the L1/L5 IFCB can be converted into the L5-only and L1/L2/L5 IF IFCB. Nevertheless, the derived IFCB relationships adopt only to the triple-frequency observations. The relationships of IFCB for even more frequency combinations such as quad- and five-frequency combinations have not been validated.

This study starts with the general GNSS equations and presents the carrier phase time-variant OSB definition. The carrier phase time-variant OSB concept is first present in this study, and the main advantage is that it can be directly corrected in the GNSS raw carrier phase observation, and the effect of the carrier phase IFCB can be eliminated in multi-frequency PPP. The carrier phase time-variant OSB can be viewed as the undifferenced bias form of the carrier phase IFCB. Subsequently, the various multi-frequency PPP models that need to take the carrier phase time-variant OSB into account are proposed, including the dual-, triple-, quad-, and five-frequency PPP models. The GNSS carrier phase time-variant OSB characteristics and positioning performance of the multi-frequency PPP models are analyzed using the datasets collected from 144 distributed MGEX stations covering one month. Finally, the conclusions are summarized.

Methodology

We first present the equations of the GNSS pseudorange and carrier phase observables. Then, the definition and estimation method of the carrier phase time-variant OSB are introduced. At last, the multi-frequency PPP models are presented.

General observation equations

Considering the time-variant characteristics of the satellite carrier phase hardware delay, the GNSS original pseudorange and carrier phase observations for the satellite s and receiver r at epoch t read (Leick et al. 2015):

$$\begin{cases} p^s_{r,j}(t) = \rho^s_r(t) + dt_r(t) - dt^s(t) + T^s_r(t) + \mu_j \cdot I^s_{r,1}(t) + d_{r,j} - d^s_j + \varepsilon^s_{p,j}(t) \\ \phi^s_{r,j}(t) = \rho^s_r(t) + dt_r(t) - dt^s(t) + T^s_r(t) - \mu_j \cdot I^s_{r,1}(t) + b_{r,j} - b^s_{c,j} - b^s_{v,j}(t) + N^s_{r,j} + \varepsilon^s_{\phi,j}(t) \end{cases} \tag{1}$$

where $p^s_{r,j}(t)$ and $\phi^s_{r,j}(t)$ denote the pseudorange and carrier phase observables; $\rho^s_r(t)$ denotes the satellite and receiver geometrical range; $dt_r(t)$ and $dt^s(t)$ denote the receiver and satellite GNSS clock offsets; $T^s_r(t)$ denotes the line-of-sight tropospheric delay; $I^s_{r,1}(t)$ denotes the line-of-sight GPS L1-based slant ionospheric delay; μ_j denotes the frequency-dependent multiplier factor; $d_{r,j}$ and d^s_j denote the receiver and satellite uncalibrated code delays (UCDs); $b_{r,j}$ denotes the receiver UPD; $b^s_{c,j}$ and $b^s_{v,j}$ denote the satellite time-invariant and time-variant UPD. The time-variant receiver UPD is ignored for the geometry-free (GF) and IF (GFIF) linear combination of the satellite and receiver UPD exhibits the consistent variations for the different stations (Pan et al. 2017b; Zhang et al. 2017). Owing to that, the pseudorange observation weight is much smaller than the phase observations in precise positioning, and thus, the UCD time-variant characteristics are ignored as well. $N^s_{r,j}$ denotes the integer ambiguity, and $\varepsilon^s_{p,j}(t)$ and $\varepsilon^s_{\phi,j}(t)$ denote the pseudorange and carrier phase measurement noises, respectively.

Definition of the carrier phase time-variant OSB

Generally, the estimated IF satellite clock will absorb the UCD and time-variant UPD in satellite PCE. Hence, the estimated satellite clock parameters read (Li et al. 2020b):

$$dt^s_{IF,12}(t) = dt^s(t) + d^s_{,IF,12} + b^s_{v,IF,12}(t) \tag{2}$$

where $(\cdot)_{IF,ij} = -\mu^{-1}_{GF,ij}\left[\mu_j, -\mu_i\right] \cdot \left[(\cdot)_i, (\cdot)_j\right]^T = \left[\alpha_{ij}, \beta_{ij}\right] \cdot \left[(\cdot)_i, (\cdot)_j\right]^T$ denotes the IF combined operation.

The satellite clock offsets absorbed with the specific IF hardware delays make the measurement inconsistent at different frequencies. The multi-frequency PPP users can determine the estimable biases at the third and beyond frequency or correct the specific hardware bias so as to obtain consistent satellite clock offsets. The transformation formula can be expressed as:

$$\begin{cases} dt^s_{IF,1}(t) = dt^s_{IF,12}(t) + \beta_{UC,1} + \delta_{UC,1}(t) \\ dt^s_{IF,2}(t) = dt^s_{IF,12}(t) + \beta_{UC,2} + \delta_{UC,2}(t) \\ dt^s_{IF,i}(t) = dt^s_{IF,12}(t) + \beta_{UC,i} + \delta_{UC,i}(t), i \in [3, +\infty) \end{cases} \tag{3}$$

where $dt^s_{IF,i}(t)$ denotes the specific satellite clock for the ith frequency signal; $\beta_{UC,i}$ denotes the ith frequency pseudorange OSB, which can be computed by the corresponding DCB values; in analogy, we can also define $\delta_{UC,i}(t)$ as the ith frequency carrier phase time-variant OSB.

With the available specific satellite clock, the arbitrarily multi-frequency uncombined PPP model is described as (Erol et al. 2020):

$$\begin{cases} \overline{p}^s_{r,1}(t) = \boldsymbol{u}^s_r(t) \cdot \boldsymbol{x}(t) + mf^s_r(t) \cdot \mathrm{ZWD}_r(t) + \overline{dt}_r(t) + \overline{I}^s_{r,1}(t) + \varepsilon^s_{p,1}(t) \\ \overline{p}^s_{r,2}(t) = \boldsymbol{u}^s_r(t) \cdot \boldsymbol{x}(t) + mf^s_r(t) \cdot \mathrm{ZWD}_r(t) + \overline{dt}_r(t) + \mu_2 \cdot \overline{I}^s_{r,1}(t) + \varepsilon^s_{p,2}(t) \\ \overline{p}^s_{r,i}(t) = \boldsymbol{u}^s_r(t) \cdot \boldsymbol{x}(t) + mf^s_r(t) \cdot \mathrm{ZWD}_r(t) + \overline{dt}_r(t) + \mu_i \cdot I^s_{r,1}(t) + ifb_i + \varepsilon^s_{p,i}(t), i \in [3, +\infty) \\ \overline{\phi}^s_{r,1}(t) = \boldsymbol{u}^s_r(t) \cdot \boldsymbol{x}(t) + mf^s_r(t) \cdot \mathrm{ZWD}_r(t) + \overline{dt}_r(t) - \overline{I}^s_{r,1}(t) + \overline{N}^s_{r,1} - \delta_{UC,1}(t) + \varepsilon^s_{\phi,1}(t) \\ \overline{\phi}^s_{r,2}(t) = \boldsymbol{u}^s_r(t) \cdot \boldsymbol{x}(t) + mf^s_r(t) \cdot \mathrm{ZWD}_r(t) + \overline{dt}_r(t) - \mu_2 \cdot \overline{I}^s_{r,1}(t) + \overline{N}^s_{r,2} - \delta_{UC,2}(t) + \varepsilon^s_{\phi,2}(t) \\ \overline{\phi}^s_{r,i}(t) = \boldsymbol{u}^s_r(t) \cdot \boldsymbol{x}(t) + mf^s_r(t) \cdot \mathrm{ZWD}_r(t) + \overline{dt}_r(t) - \mu_i \cdot \overline{I}^s_{r,1}(t) + \overline{N}^s_{r,i} - \delta_{UC,i}(t) + \varepsilon^s_{\phi,i}(t), i \in [3, +\infty) \end{cases} \tag{4}$$

with

$$\begin{cases} \overline{dt}_r(t) = dt_r(t) + d_{r,IF,12} \\ \overline{I}^s_{r,1}(t) = I^s_{r,1}(t) + \mu^{-1}_{GF,12} \cdot d_{r,GF,12} + \mu^{-1}_{GF,12} \cdot b^s_{v,GF,12}(t) \\ ifb_i = \beta_{12}/\beta_{1i} \cdot d_{r,GF,12} - d_{r,GF,1i}, i \in [3, +\infty) \\ \overline{N}^s_{r,i} = N^s_{r,i} + b_{r,i} - b^s_{,i} - d_{r,IF,12} + \mu_i \cdot \mu^{-1}_{GF,12} \cdot d_{r,GF,12}, i \in [1, +\infty) \end{cases} \tag{5}$$

where ifb_i denotes the ith frequency receiver pseudorange interfrequency bias (IFB). The estimated ionospheric delay in the multi-frequency uncombined PPP model contains the receiver IF UCD and time-variant UPD. Hence, the carrier phase time-variant OSB values at the first and second frequency signals are equal to zero. Since the observations on all bands share the same estimated ionospheric parameters, the carrier phase time-variant OSB values on other frequencies are not zero. The carrier phase time-variant OSB is ignored in the pseudorange

observations, for the pseudorange noise is far more than that of the carrier phase observations.

According to the above equations, the multi-frequency carrier phase time-variant OSB is expressed as:

$$\begin{cases} \delta^s_{UC,1}(t) = 0 \\ \delta^s_{UC,2}(t) = 0 \\ \delta^s_{UC,i}(t) = \alpha_{12} \cdot (\mu_i/\mu_2 - 1) \cdot b^s_{v,1}(t) + \beta_{12} \cdot (\mu_i - 1) \cdot b^s_{v,2}(t) + b^s_{v,i}(t), i \in [3, +\infty) \end{cases} \tag{6}$$

Equation (6) indicates that the carrier phase time-variant OSB is composed of the time-variant UPD at different frequencies.

Rationality of the carrier phase time-variant OSB concept

The first-order ionospheric delay can be eliminated with the IF combination. Consequently, the carrier phase IFCB values between L1/Li and L1/L2 and between Li/Lj and L1/L2 are written as:

$$\begin{cases} \delta^s_{IF,1i}(t) = b^s_{v,IF,1i}(t) - b^s_{v,IF,12}(t) = (\alpha_{1i} - \alpha_{12}) \cdot b^s_{v,1}(t) - \beta_{12} \cdot b^s_{v,2}(t) + \beta_{1i} \cdot b^s_{v,i}(t) = \alpha_{1i} \cdot \delta^s_{UC,1}(t) + \beta_{1i} \cdot \delta^s_{UC,i}(t), i \in [3, +\infty) \\ \delta^s_{IF,ij}(t) = b^s_{v,IF,ij}(t) - b^s_{v,IF,12}(t) = -\alpha_{12} \cdot b^s_{v,1}(t) - \beta_{12} \cdot b^s_{v,2}(t) + \alpha_{ij} \cdot b^s_{v,i}(t) + \beta_{ij} \cdot b^s_{v,j}(t) = \alpha_{ij} \cdot \delta^s_{UC,i}(t) + \beta_{ij} \cdot \delta^s_{UC,j}(t), i,j \in [3, +\infty), i < j \end{cases} \tag{7}$$

The above equations indicate that the IF carrier phase IFCB can be viewed as the linear relation of the carrier phase time-variant OSB at different frequencies.

The k frequency measurements can be integrated into one observation. The two basic necessary requirements to determine the combined coefficients are eliminating the first-order ionospheric delay and keeping the geometric distance unchanged, which are expressed as:

$$\begin{cases} \sum_{i=1}^{k} \eta_i = 1 \\ \sum_{i=1}^{k} \eta_i \cdot \mu_i = 0 \end{cases} \tag{8}$$

The two basic conditions do not satisfy the requirements to determine the required combined coefficients. The third condition, such as wavelength length, cycle ambiguity characteristic, and minimum combination noise, can determine the combined coefficient. The carrier phase IFCB values between the k frequency IF observation and L1/L2 IF observation are expressed as:

$$\begin{aligned} &\delta_{IF,12\cdots k}(t) = b^s_{v,IF,12\cdots k}(t) - b^s_{v,IF,12}(t) \\ &= (\eta_1 - \alpha_{12}) \cdot b^s_{v,1}(t) + (\eta_2 - \beta_{12}) \cdot b^s_{v,2}(t) \\ &+ \sum_{i=3}^{k} \eta_i \cdot b^s_{v,i}(t) = \sum_{i=1}^{k} c_i \cdot b^s_{v,i}(t) \end{aligned} \tag{9}$$

where c_i denotes the combined coefficient of the carrier phase time-variant UPD, which satisfies the following conditions:

$$\begin{cases} \sum_{i=1}^{k} c_i = 0 \\ \sum_{i=1}^{k} c_i \cdot \mu_i = 0 \end{cases} \tag{10}$$

With the above conditions, the c_1 and c_2 coefficients can be further expressed as:

$$\begin{cases} c_1 = \sum_{i=3}^{k} \frac{\mu_i - \mu_2}{\mu_2 - \mu_1} \cdot c_i \\ c_2 = \sum_{i=3}^{k} \frac{1 - \mu_i}{\mu_2 - \mu_1} \cdot c_i \end{cases} \tag{11}$$

Substituting the (11) into (9), we can derive the following relationship:

$$\delta^s_{IF,12\cdots k}(t) = \sum_{i=3}^{k} \left[\left(\frac{\mu_i - \mu_2}{\mu_2 - \mu_1} \cdot b^s_{v,1}(t) + \frac{1 - \mu_i}{\mu_2 - \mu_1} \cdot b^s_{v,2}(t) + b^s_{v,i}(t) \right) \cdot c_i \right] = \sum_{i=1}^{k} \left[\delta^s_{UC,i}(t) \cdot \eta_i \right] \tag{12}$$

Consistent with the dual-frequency IF IFCB, the multi-frequency IF IFCB is also made up of the carrier phase time-variant OSB combination at each frequency. We have defined the carrier phase IFCB with respect to the uncombined observations as the carrier phase time-variant OSB. The readers are probably confused about the carrier phase time-variant OSB with the use of such a concept in generating IFCB. To verify the adequacy of the OSB concept, we check the OSB definition as described in the SINEX_BIAS Version 1.00 and the relationship of the OSB and IF bias reads (Schaer 2016):

$$(\cdot)_{IF,ij} = \alpha_{ij} \cdot (\cdot)_i + \beta_{ij} \cdot (\cdot)_j \tag{13}$$

Strictly following the above equation, the bias with respect to the IF case for the carrier phase time-variant hardware delay refers to the IFCB. Equations (9) and (12) indicate that the defined carrier phase time-variant OSB parameters satisfy the parameter transformed requirement from OSB to IF bias. Hence, the carrier phase time-variant OSB definition is reasonable and beneficial for the GNSS community. More conveniently, the carrier phase time-variant OSB can be directly applied in the raw carrier phase observation, and thereafter, the carrier phase time-variant UPD can be eliminated.

When the carrier phase time-variant OSB at each frequency is available, we can apply the transformed equations to obtain the multi-frequency carrier phase IFCB and the covariance propagation rate to calculate the IFCB confidence.

Numerical approach of the carrier phase time-variant OSB

To improve the computational efficiency and meet the requirements of timeliness, we adopted the epoch-difference approach to calculate the carrier phase time-variant OSB, where the L1/L*i* and L1/L2 phase IFCB can be obtained by GFIF combination. The epoch-difference approach reads:

$$\phi^s_{r,DIF,12i}(t) = \phi^s_{r,IF,12}(t) - \phi^s_{r,IF,1i}(t) = \delta_{IF,1i}(t) + \overline{N}^s_{r,DIF,12i}(t) \tag{14}$$

where $\overline{N}^s_{r,DIF,12i}(t)$ denotes the differential IF carrier phase ambiguity.

Reorganizing the above formula, we can obtain:

$$\delta^s_{r,IF,1i}(t) = \phi^s_{r,DIF,12i}(t) - \overline{N}^s_{r,DIF,12i}(t) \tag{15}$$

The above equation indicates that IF carrier phase IFCB is composed of the corresponding phase observation and ambiguity. In the case of no cycle slip occurring, the ambiguity can be eliminated with the epoch-difference strategy, which is expressed as:

$$\Delta\delta^s_{r,IF,1i}(t,t-1) = \phi^s_{r,DIF,12i}(t) - \phi^s_{r,DIF,12i}(t-1) \tag{16}$$

where $\Delta\delta^s_{r,IF,1i}(t,t-1)$ denotes the differential IF carrier phase IFCB for the pair receiver r and satellite s at epoch t.

Assuming that satellite s can be observed by n common viewing stations in the observational network at epochs t and t-1, the epoch-differenced carrier phase IFCB is expressed as:

$$\begin{cases} \Delta\delta^s_{IF,1i}(t,t-1) = \dfrac{\sum_{r=1}^{n}\left[\Delta\delta^s_{r,IF,1i}(t,t-1)\cdot\omega^s_r(t,t-1)\right]}{\sum_{r=1}^{n}\left[\omega^s_r(t,t-1)\right]} \\ \omega^s_r(t,t-1) = \begin{cases} \sin(\omega^s_r(t,t-1)), E^s_r(t,t-1) < 40^\circ \\ 1, E^s_r(t,t-1) \geq 40^\circ \end{cases} \end{cases} \tag{17}$$

where $E^s_r(t,t-1)$ denotes the average elevation of satellite s at epoch t and t-1. Consequently, the IF carrier phase phase IFCB can be accumulated by the epoch-differenced IFCB, which reads:

$$\delta^s_{IF,1i}(t) = \delta^s_{IF,1i}(t_0) + \sum_{i=t_0+1}^{t} \Delta\delta^s_{IF,1i}(t,t-1) \tag{18}$$

where t_0 denotes the initial epoch time, in which the IFCB value with respect to the first epoch is set to zero. Owing to carrier phase time-variant OSB at the first frequency is zero, the relationship of the ith frequency carrier phase time-variant OSB and the carrier phase IFCB can be expressed as:

$$\delta^s_{UC,i}(t) = \delta^s_{IF,1i}(t)/\beta_{1i} \tag{19}$$

Hence, the carrier phase time-variant OSB at all frequencies can be derived.

Multi-frequency PPP models

This section presents two dual-frequency, three triple-frequency, three quad-frequency, and three five-frequency PPP models (Su and Jin 2021). Table 1 gives the linearized model of the multi-frequency PPP, in which carrier phase time-variant OSB can be directly corrected on the raw phase observation. The corresponding multi-frequency PPP models assume observing the number of m satellites. For the expression convenience, we define the following notations:

$$\begin{cases} (\cdot)_{IF,ijk} = \left[\eta_i, \eta_j, \eta_k\right] \cdot \left[(\cdot)_i, (\cdot)_j, (\cdot)_k\right]^T \\ (\cdot)_{IF,ijkl} = \left[\eta_i, \eta_j, \eta_k, \eta_l\right] \cdot \left[(\cdot)_i, (\cdot)_j, (\cdot)_k, (\cdot)_l\right]^T \\ (\cdot)_{IF,ijklo} = \left[\eta_i, \eta_j, \eta_k, \eta_l, \eta_o\right] \cdot \left[(\cdot)_i, (\cdot)_j, (\cdot)_k, (\cdot)_l, (\cdot)_o\right]^T \end{cases} \tag{20}$$

where η denotes the corresponding multi-frequency combined coefficient.

Experimental data and processing strategies

To estimate the reliable carrier phase time-variant OSB and evaluate the effect on GNSS multi-frequency PPP, 144 MGEX stations collected during the day of year (DOY) 275–305, 2020 are utilized to conduct the experiment. The selected stations can all observe the multi-frequency GNSS signals. The Asia–Pacific regional stations can observe the QZSS signals. Figure 1 depicts the geometrical distribution of the selected MGEX stations. Among it, 70 stations can observe at least 4 BDS-2 satellites, 74 stations can track the BDS-3 B1I/B3I/BIC/B2a signals, and 20 stations can track the BDS-3 B1I/B3I/BIC/B2a/B2b/B2 signals, which are also marked in Fig. 1. Table 2 lists the observed multi-frequency signals of the GPS, BDS, Galileo and QZSS, which are the potential targets for the carrier phase time-variant OSB estimation. The selected MGEX stations are used for the GPS, BDS-2, BDS-3, Galileo and QZSS carrier phase time-variant OSB estimation. To evaluate the effect of the carrier phase time-variant OSB on multi-frequency PPP, the GNSS multi-frequency PPP solutions are conducted, including the GPS L1/L2 DF1 and DF2, GPS L1/L2/L5 TF1, TF2 and TF3, BDS-2 B1I/B2I DF1 and DF2, BDS-2 B1I/B2I/B3I TF1, TF2 and TF3, BDS-3 B1C/B2a DF1 and DF2, BDS-3 B1I/B3I/B2a TF1, TF2 and TF3, BDS-3 B1I/B3I/B1C/B2a

Table 1 Linearized equations of the dual-, triple-, quad- and five-frequency PPP models

Models	Equations	Notations
DF1: dual-frequency ionospheric-float PPP	$\begin{cases} \begin{bmatrix} \boldsymbol{P}_{DF1,ij} \\ \boldsymbol{\Phi}_{DF1,ij} \end{bmatrix} = \left[\boldsymbol{e}_4 \otimes \boldsymbol{G}_r, \boldsymbol{e}_{4m}, \boldsymbol{n}_2 \otimes \boldsymbol{\mu}_2 \otimes \boldsymbol{I}_m, z_2 \otimes \boldsymbol{I}_{2m}\right] \cdot \boldsymbol{\xi}_{DF1} + \begin{bmatrix} \boldsymbol{\varepsilon}_{\boldsymbol{P}_{DF1,ij}} \\ \boldsymbol{\varepsilon}_{\boldsymbol{\Phi}_{DF1,ij}} \end{bmatrix}, \\ \boldsymbol{q}_2 \otimes \boldsymbol{Q}_r \otimes \boldsymbol{Q}_m \end{cases}$	$\boldsymbol{P}_{DF1,ij} = \left[p^1_{r,i}(t), p^2_{r,i}(t), \ldots, p^m_{r,j}(t)\right]^T$; $\boldsymbol{\Phi}_{DF1,ij} = \left[\phi^1_{r,i}(t), \phi^2_{r,i}(t), \ldots, \phi^m_{r,j}(t)\right]^T$; $\boldsymbol{\xi}_{DF1} = \left[\boldsymbol{x}, \mathrm{ZWD}_r(t), d\bar{t}_r(t), \boldsymbol{\tau}, \boldsymbol{a}_2\right]^T$; $\boldsymbol{\tau} = \left[\bar{I}^1_{r,1}(t), \ldots, \bar{I}^m_{r,1}(t)\right]^T$; $\boldsymbol{a}_2 = \left[\overline{N}^1_{r,i}(t), \overline{N}^2_{r,i}(t), \ldots, \overline{N}^m_{r,j}(t)\right]^T$
DF2: dual-frequency IF PPP	$\begin{cases} \begin{bmatrix} \boldsymbol{P}_{DF2,ij} \\ \boldsymbol{\Phi}_{DF2,ij} \end{bmatrix} = \left[\boldsymbol{e}_2 \otimes \boldsymbol{G}_r, \boldsymbol{e}_{2m}, z_2 \otimes \boldsymbol{I}_m\right] \cdot \boldsymbol{\xi}_{DF2} + \begin{bmatrix} \boldsymbol{\varepsilon}_{\boldsymbol{P}_{DF2,ij}} \\ \boldsymbol{\varepsilon}_{\boldsymbol{\Phi}_{DF2,ij}} \end{bmatrix}, \\ \boldsymbol{\eta}_2^T \cdot \boldsymbol{q}_2 \cdot \boldsymbol{\eta}_2 \otimes \boldsymbol{Q}_r \otimes \boldsymbol{Q}_m \end{cases}$	$\boldsymbol{P}_{DF2,ij} = \boldsymbol{P}_{IF,ij}$; $\boldsymbol{\Phi}_{DF2,ij} = \boldsymbol{\Phi}_{IF,ij}$; $\boldsymbol{\xi}_{DF2} = \left[\boldsymbol{x}, \mathrm{ZWD}_r(t), d\bar{t}_r(t), \boldsymbol{a}_1\right]^T$; $\boldsymbol{a}_1 = \left[\overline{N}^1_{r,IF,ij}(t), \ldots, \overline{N}^m_{r,IF,ij}(t)\right]^T$
TF1: triple-frequency ionospheric-float PPP	$\begin{cases} \begin{bmatrix} \boldsymbol{P}_{TF1,ijk} \\ \boldsymbol{\Phi}_{TF1,ijk} \end{bmatrix} = \left[\boldsymbol{e}_6 \otimes \boldsymbol{G}_r, \boldsymbol{e}_{6m}, \boldsymbol{v}_2 \otimes z_3 \otimes \boldsymbol{e}_m, \boldsymbol{n}_2 \otimes \boldsymbol{\mu}_3 \otimes \boldsymbol{I}_m, z_2 \otimes \boldsymbol{I}_{3m}\right] \cdot \boldsymbol{\xi}_{TF1} + \begin{bmatrix} \boldsymbol{\varepsilon}_{\boldsymbol{P}_{TF1,ijk}} \\ \boldsymbol{\varepsilon}_{\boldsymbol{\Phi}_{TF1,ijk}} \end{bmatrix}, \\ \boldsymbol{q}_3 \otimes \boldsymbol{Q}_r \otimes \boldsymbol{Q}_m \end{cases}$	$\boldsymbol{P}_{TF1,ijk} = \left[p^1_{r,i}(t), p^2_{r,i}(t), \ldots, p^m_{r,j}(t), \ldots, p^m_{r,k}(t)\right]^T$; $\boldsymbol{\Phi}_{TF1,ijk} = \left[\phi^1_{r,i}(t), \phi^2_{r,i}(t), \ldots, \phi^m_{r,j}(t), \ldots, \phi^m_{r,k}(t)\right]^T$; $\boldsymbol{\xi}_{TF1} = \left[\boldsymbol{x}, \mathrm{ZWD}_r(t), d\bar{t}_r(t), ifb_{TF1}, \boldsymbol{\tau}, \boldsymbol{a}_3\right]^T$; $\boldsymbol{a}_3 = \left[\overline{N}^1_{r,i}(t), \overline{N}^2_{r,i}(t), \ldots, \overline{N}^m_{r,j}(t), \ldots, \overline{N}^m_{r,k}(t)\right]^T$;
TF2: triple-frequency IF PPP of two combinations	$\begin{cases} \begin{bmatrix} \boldsymbol{P}_{TF2,ijk} \\ \boldsymbol{\Phi}_{TF2,ijk} \end{bmatrix} = \left[\boldsymbol{e}_4 \otimes \boldsymbol{G}_r, \boldsymbol{e}_{4m}, \boldsymbol{v}_2 \otimes z_2 \otimes \boldsymbol{e}_m, z_2 \otimes \boldsymbol{I}_{2m}\right] \cdot \boldsymbol{\xi}_{TF2} + \begin{bmatrix} \boldsymbol{\varepsilon}_{\boldsymbol{P}_{TF2,ijk}} \\ \boldsymbol{\varepsilon}_{\boldsymbol{\Phi}_{TF2,ijk}} \end{bmatrix}, \\ \boldsymbol{\kappa}_3^T \cdot \boldsymbol{q}_3 \cdot \boldsymbol{\kappa}_3 \otimes \boldsymbol{Q}_r \otimes \boldsymbol{Q}_m, \end{cases}$	$\boldsymbol{P}_{TF2,ijk} = \left[\boldsymbol{P}_{IF,ij}, \boldsymbol{P}_{IF,ik}\right]^T$; $\boldsymbol{\Phi}_{TF2,ijk} = \left[\boldsymbol{\Phi}_{IF,ij}, \boldsymbol{\Phi}_{IF,ik}\right]^T$; $\boldsymbol{\xi}_{TF2} = \left[\boldsymbol{x}, \mathrm{ZWD}_r(t), d\bar{t}_r(t), ifb_{TF2}, \boldsymbol{a}_2\right]^T$; $\boldsymbol{a}_2 = \left[\overline{N}^1_{r,IF,ij}(t), \ldots, \overline{N}^m_{r,IF,ij}(t), \ldots, \overline{N}^m_{r,IF,ik}(t)\right]^T$
TF3: triple-frequency IF PPP of one combination	$\begin{cases} \begin{bmatrix} \boldsymbol{P}_{TF3,ijk} \\ \boldsymbol{\Phi}_{TF3,ijk} \end{bmatrix} = \left[\boldsymbol{e}_2 \otimes \boldsymbol{G}_r, \boldsymbol{e}_{2m}, z_2 \otimes \boldsymbol{I}_m\right] \cdot \boldsymbol{\xi}_{TF3} + \begin{bmatrix} \boldsymbol{\varepsilon}_{\boldsymbol{P}_{TF3,ijk}} \\ \boldsymbol{\varepsilon}_{\boldsymbol{\Phi}_{TF3,ijk}} \end{bmatrix}, \\ \boldsymbol{\eta}_3^T \cdot \boldsymbol{q}_3 \cdot \boldsymbol{\eta}_3 \otimes \boldsymbol{Q}_r \otimes \boldsymbol{Q}_m \end{cases}$	$\boldsymbol{P}_{TF3,ijk} = \boldsymbol{P}_{IF,ijk}$; $\boldsymbol{\Phi}_{TF3,ijk} = \boldsymbol{\Phi}_{IF,ijk}$; $\boldsymbol{\xi}_{TF3} = \left[\boldsymbol{x}, \mathrm{ZWD}_r(t), d\bar{t}_r(t), \boldsymbol{a}_1\right]^T$; $\boldsymbol{a}_1 = \left[\overline{N}^1_{r,IF,ijk}(t), \ldots, \overline{N}^m_{r,IF,ijk}(t)\right]^T$;
QF1: quad-frequency ionospheric-float PPP	$\begin{cases} \begin{bmatrix} \boldsymbol{P}_{QF1,ijkl} \\ \boldsymbol{\Phi}_{QF1,ijkl} \end{bmatrix} = \left[\boldsymbol{e}_8 \otimes \boldsymbol{G}_r, \boldsymbol{e}_{8m}, \boldsymbol{v}_2 \otimes z_4 \otimes \boldsymbol{e}_m, \boldsymbol{n}_2 \otimes \boldsymbol{\mu}_4 \otimes \boldsymbol{I}_m, z_2 \otimes \boldsymbol{I}_{4m}\right] \cdot \boldsymbol{\xi}_{QF1} + \begin{bmatrix} \boldsymbol{\varepsilon}_{\boldsymbol{P}_{QF1,ijkl}} \\ \boldsymbol{\varepsilon}_{\boldsymbol{\Phi}_{QF1,ijkl}} \end{bmatrix}, \\ \boldsymbol{q}_4 \otimes \boldsymbol{Q}_r \otimes \boldsymbol{Q}_m \end{cases}$	$\boldsymbol{P}_{QF1,ijkl} = \left[p^1_{r,i}(t), p^2_{r,i}(t), \ldots, p^m_{r,j}(t), \ldots, p^m_{r,k}(t), \ldots, p^m_{r,l}(t)\right]^T$; $\boldsymbol{\Phi}_{QF1,ijkl} = \left[\phi^1_{r,i}(t), \phi^2_{r,i}(t), \ldots, \phi^m_{r,j}(t), \ldots, \phi^m_{r,k}(t), \ldots, \phi^m_{r,l}(t)\right]^T$; $\boldsymbol{\xi}_{QF1} = \left[\boldsymbol{x}, \mathrm{ZWD}_r(t), d\bar{t}_r(t), ifb_{QF1,k}, ifb_{QF1,l}, \boldsymbol{\tau}, \boldsymbol{a}_4\right]^T$; $\boldsymbol{a}_4 = \left[\overline{N}^1_{r,i}(t), \overline{N}^2_{r,i}(t), \ldots, \overline{N}^m_{r,j}(t), \ldots, \overline{N}^m_{r,k}(t), \ldots, \overline{N}^m_{r,l}(t)\right]^T$;

Table 1 (continued)

Models	Equations	Notations
QF2: quad-frequency IF PPP of two combinations	$\begin{cases} \begin{bmatrix} \boldsymbol{P}_{QF2,ijkl} \\ \boldsymbol{\Phi}_{QF2,ijkl} \end{bmatrix} = \left[\boldsymbol{e}_4 \otimes \boldsymbol{G}_r, \boldsymbol{e}_{4m}, \boldsymbol{v}_2 \otimes z_2 \otimes \boldsymbol{e}_m, z_2 \otimes \boldsymbol{I}_{2m}\right] \cdot \boldsymbol{\xi}_{QF2} + \begin{bmatrix} \boldsymbol{\varepsilon}_{\boldsymbol{P}_{QF2,ijkl}} \\ \boldsymbol{\varepsilon}_{\boldsymbol{\Phi}_{QF2,ijkl}} \end{bmatrix}, \\ \boldsymbol{\kappa}_4^T \cdot \boldsymbol{q}_4 \cdot \boldsymbol{\kappa}_4 \otimes \boldsymbol{Q}_r \otimes \boldsymbol{Q}_m \end{cases}$	$\boldsymbol{P}_{QF2,ijkl} = \left[\boldsymbol{P}_{IF,ij}, \boldsymbol{P}_{IF,kl}\right]^T; \boldsymbol{\Phi}_{QF2,ijkl} = \left[\boldsymbol{\Phi}_{IF,ij}, \boldsymbol{\Phi}_{IF,kl}\right]^T;$ $\boldsymbol{\xi}_{QF2} = \left[\boldsymbol{x}, \mathrm{ZWD}_r(t), d\bar{t}_r(t), ifb_{QF2}, \boldsymbol{a}_2\right]^T;$ $\boldsymbol{a}_2 = \left[\overline{N}^1_{r,IF,ij}(t), \ldots, \overline{N}^m_{r,IF,ij}(t), \ldots, \overline{N}^m_{r,IF,kl}(t)\right]^T;$
QF3: quad-frequency IF PPP of one combination	$\begin{cases} \begin{bmatrix} \boldsymbol{P}_{QF3,ijkl} \\ \boldsymbol{\Phi}_{QF3,ijkl} \end{bmatrix} = \left[\boldsymbol{e}_2 \otimes \boldsymbol{G}_r, \boldsymbol{e}_{2m}, z_2 \otimes \boldsymbol{I}_m\right] \cdot \boldsymbol{\xi}_{QF3} + \begin{bmatrix} \boldsymbol{\varepsilon}_{\boldsymbol{P}_{QF3,ijkl}} \\ \boldsymbol{\varepsilon}_{\boldsymbol{\Phi}_{QF3,ijkl}} \end{bmatrix}, \\ \boldsymbol{\eta}_4^T \cdot \boldsymbol{q}_4 \cdot \boldsymbol{\eta}_4 \otimes \boldsymbol{Q}_r \otimes \boldsymbol{Q}_m \end{cases}$	$\boldsymbol{P}_{QF3,ijkl} = \boldsymbol{P}_{IF,ijkl}; \boldsymbol{\Phi}_{QF3,ijkl} = \boldsymbol{\Phi}_{IF,ijkl}; \boldsymbol{\xi}_{QF3} = \left[\boldsymbol{x}, \mathrm{ZWD}_r(t), d\bar{t}_r(t), \boldsymbol{a}_1\right]^T;$ $\boldsymbol{a}_1 = \left[\overline{N}^1_{r,IF,ijkl}(t), \ldots, \overline{N}^m_{r,IF,ijkl}(t)\right]^T;$
FF1: five-frequency ionospheric-float PPP	$\begin{cases} \begin{bmatrix} \boldsymbol{P}_{FF1,ijklo} \\ \boldsymbol{\Phi}_{FF1,ijklo} \end{bmatrix} = \left[\boldsymbol{e}_{10} \otimes \boldsymbol{G}_r, \boldsymbol{e}_{10m}, \boldsymbol{v}_2 \otimes z_5 \otimes \boldsymbol{e}_m, \boldsymbol{n}_2 \otimes \boldsymbol{\mu}_5 \otimes \boldsymbol{I}_m, z_2 \otimes \boldsymbol{I}_{5m}\right] \cdot \boldsymbol{\xi}_{FF1} + \begin{bmatrix} \boldsymbol{\varepsilon}_{\boldsymbol{P}_{FF1,ijklo}} \\ \boldsymbol{\varepsilon}_{\boldsymbol{\Phi}_{FF1,ijklo}} \end{bmatrix}, \\ \boldsymbol{q}_5 \otimes \boldsymbol{Q}_r \otimes \boldsymbol{Q}_m \end{cases}$	$\boldsymbol{P}_{FF1,ijklo} = \left[p^1_{r,i}(t), p^2_{r,i}(t), \ldots, p^m_{r,j}(t), \ldots, p^m_{r,k}(t), \ldots, p^m_{r,l}(t), \ldots, p^m_{r,o}(t)\right]^T;$ $\boldsymbol{\Phi}_{FF1,ijklo} = \left[\phi^1_{r,i}(t), \phi^2_{r,i}(t), \ldots, \phi^m_{r,j}(t), \ldots, \phi^m_{r,k}(t), \ldots, \phi^m_{r,l}(t), \ldots, \phi^m_{r,o}(t)\right]^T;$ $\boldsymbol{\xi}_{FF1} = \left[\boldsymbol{x}, \mathrm{ZWD}_r(t), d\bar{t}_r(t), ifb_{FF1,k}, ifb_{FF1,l}, ifb_{FF1,o}, \boldsymbol{\tau}, \boldsymbol{a}_5\right]^T;$ $\boldsymbol{a}_5 = \left[\overline{N}^1_{r,i}(t), \overline{N}^2_{r,i}(t), \ldots, \overline{N}^m_{r,j}(t), \ldots, \overline{N}^m_{r,k}(t), \ldots, \overline{N}^m_{r,l}(t), \ldots, \overline{N}^m_{r,o}(t)\right]^T;$
FF2: five-frequency IF PPP of four combinations	$\begin{cases} \begin{bmatrix} \boldsymbol{P}_{FF2,ijklo} \\ \boldsymbol{\Phi}_{FF2,ijklo} \end{bmatrix} = \left[\boldsymbol{e}_8 \otimes \boldsymbol{G}_r, \boldsymbol{e}_{8m}, \boldsymbol{v}_2 \otimes \boldsymbol{z'}_4 \otimes \boldsymbol{e}_m, z_2 \otimes \boldsymbol{I}_{4m}\right] \cdot \boldsymbol{\xi}_{FF2} + \begin{bmatrix} \boldsymbol{\varepsilon}_{\boldsymbol{P}_{FF2,ijklo}} \\ \boldsymbol{\varepsilon}_{\boldsymbol{\Phi}_{FF2,ijklo}} \end{bmatrix}, \\ \boldsymbol{\kappa}_5^T \cdot \boldsymbol{q}_5 \cdot \boldsymbol{\kappa}_5 \otimes \boldsymbol{Q}_r \otimes \boldsymbol{Q}_m \end{cases}$	$\boldsymbol{P}_{FF2,ijklo} = \left[\boldsymbol{P}_{IF,ij}, \boldsymbol{P}_{IF,ik}, \boldsymbol{P}_{IF,il}, \boldsymbol{P}_{IF,io}\right]^T;$ $\boldsymbol{\Phi}_{FF2,ijklo} = \left[\boldsymbol{\Phi}_{IF,ij}, \boldsymbol{\Phi}_{IF,ik}, \boldsymbol{\Phi}_{IF,il}, \boldsymbol{\Phi}_{IF,io}\right]^T;$ $\boldsymbol{\xi}_{FF2} = \left[\boldsymbol{x}, \mathrm{ZWD}_r(t), d\bar{t}_r(t), ifb_{FF2,k}, ifb_{FF2,l}, ifb_{FF2,o}, \boldsymbol{a}_4\right]^T;$ $\boldsymbol{a}_4 = \left[\overline{N}^1_{r,IF,ij}(t), \ldots, \overline{N}^m_{r,IF,ij}(t), \ldots, \overline{N}^m_{r,IF,ik}(t), \ldots, \overline{N}^m_{r,IF,il}(t), \ldots, \overline{N}^m_{r,IF,io}(t)\right]^T;$
FF3: five-frequency IF PPP of one combination	$\begin{cases} \begin{bmatrix} \boldsymbol{P}_{FF3,ijklo} \\ \boldsymbol{\Phi}_{FF3,ijklo} \end{bmatrix} = \left[\boldsymbol{e}_2 \otimes \boldsymbol{G}_r, \boldsymbol{e}_{2m}, z_2 \otimes \boldsymbol{I}_m\right] \cdot \boldsymbol{\xi}_{FF3} + \begin{bmatrix} \boldsymbol{\varepsilon}_{\boldsymbol{P}_{FF3,ijklo}} \\ \boldsymbol{\varepsilon}_{\boldsymbol{\Phi}_{FF3,ijklo}} \end{bmatrix}, \\ \boldsymbol{\eta}_5^T \cdot \boldsymbol{q}_5 \cdot \boldsymbol{\eta}_5 \otimes \boldsymbol{Q}_r \otimes \boldsymbol{Q}_m \end{cases}$	$\boldsymbol{P}_{FF3,ijklo} = \boldsymbol{P}_{IF,ijklo}; \boldsymbol{\Phi}_{FF3,ijklo} = \boldsymbol{\Phi}_{IF,ijklo}; \boldsymbol{\xi}_{FF3} = \left[\boldsymbol{x}, \mathrm{ZWD}_r(t), d\bar{t}_r(t), \boldsymbol{a}_1\right]^T;$ $\boldsymbol{a}_1 = \left[\overline{N}^1_{r,IF,ijklo}(t), \ldots, \overline{N}^m_{r,IF,ijklo}(t)\right]^T;$

Where $ZWD_r(t)$ denotes the tropospheric zenith wet delay (ZWD); $\boldsymbol{G}_r = \left[\boldsymbol{B}_r, \boldsymbol{M}_r\right]$, in which $\boldsymbol{B}_r$ denotes the receiver position increment design matrix, $\boldsymbol{M}_r$ denotes the tropospheric wet mapping function design matrix; $\boldsymbol{Q}_r = \mathrm{diag}(\delta_p^2, \delta_\phi^2)$ denotes the pseudorange and carrier phase zenith direction accuracy matrix; $\boldsymbol{Q}_m$ denotes satellite elevation factor matrix; $\boldsymbol{e}_m$ denotes the m-row vector, in which all values are 1; $\boldsymbol{I}_m$ denotes the m-dimension identity matrix; $\boldsymbol{n}_2 = [1, -1]^T$, $\boldsymbol{v}_2 = [1, 0]^T$, $z_2 = [0, 1]^T$, $z_3 = [0, 0, 1]^T$, $z_4 = \begin{bmatrix} 0 & 0 & 1 & 0 \\ 0 & 0 & 0 & 1 \end{bmatrix}^T$, $\boldsymbol{z'}_4 = \begin{bmatrix} 0 & 1 & 0 & 0 \\ 0 & 0 & 1 & 0 \\ 0 & 0 & 0 & 1 \end{bmatrix}^T$, $z_5 = \begin{bmatrix} 0 & 0 & 1 & 0 & 0 \\ 0 & 0 & 0 & 1 & 0 \\ 0 & 0 & 0 & 0 & 1 \end{bmatrix}^T$; $\boldsymbol{\mu}_2 = \left[\mu_i, \mu_j\right]^T$, $\boldsymbol{\mu}_3 = \left[\mu_i, \mu_j, \mu_k\right]^T$, $\boldsymbol{\mu}_4 = \left[\mu_i, \mu_j, \mu_k, \mu_l\right]^T$, $\boldsymbol{\mu}_5 = \left[\mu_i, \mu_j, \mu_k, \mu_l, \mu_o\right]^T$, $\boldsymbol{\eta}_2 = \left[\alpha_{ij}, \beta_{ij}\right]^T$, $\boldsymbol{\eta}_3 = \left[\eta_i, \eta_j, \eta_k\right]^T$, $\boldsymbol{\eta}_4 = \left[\eta_i, \eta_j, \eta_k, \eta_l\right]^T$, $\boldsymbol{\eta}_5 = \left[\eta_i, \eta_j, \eta_k, \eta_l, \eta_o\right]^T$; $\boldsymbol{\kappa}_3 = \begin{bmatrix} \alpha_{ij} & \beta_{ij} & 0 \\ \alpha_{ik} & 0 & \beta_{ik} \end{bmatrix}^T$, $\boldsymbol{\kappa}_4 = \begin{bmatrix} \alpha_{ij} & \beta_{ij} & 0 & 0 \\ 0 & 0 & \alpha_{kl} & \beta_{kl} \end{bmatrix}^T$, $\boldsymbol{\kappa}_5 = \begin{bmatrix} \alpha_{ij} & \beta_{ij} & 0 & 0 & 0 \\ \alpha_{ik} & 0 & \beta_{ik} & 0 & 0 \\ \alpha_{il} & 0 & 0 & \beta_{il} & 0 \\ \alpha_{io} & 0 & 0 & 0 & \beta_{io} \end{bmatrix}^T$; $\boldsymbol{q}_2 = \mathrm{diag}(q_i^2, q_j^2)$, $\boldsymbol{q}_3 = \mathrm{diag}(q_i^2, q_j^2, q_k^2)$, $\boldsymbol{q}_4 = \mathrm{diag}(q_i^2, q_j^2, q_k^2, q_l^2)$, $\boldsymbol{q}_5 = \mathrm{diag}(q_i^2, q_j^2, q_k^2, q_l^2, q_o^2)$, in which q_i denotes the observation noise ratio at ith frequency.

Table 2 Observed multi-frequency signals of the GPS, BDS, Galileo and QZSS

GNSS systems	PRN	Comment
GPS	G01, G03, G04, G06, G08, G09, G10, G18, G23, G24, G25, G26, G27, G30, G32	L1, L2, L5 (Block IIF)
BDS-2	C01, C02, C03, C04, C05, C06, C07, C08, C09, C10, C11, C12, C13, C14, C16	B1I, B3I, B2I
BDS-3	C19, C20, C21, C22, C23, C24, C25, C26, C27, C28, C29, C30, C32, C33, C34, C35, C36, C37, C38, C39, C40, C41, C42, C43, C44, C45, C46, C60	B1I, B3I, B1C, B2a, B2b, B2
Galileo	E01, E02, E03, E04, E05, E07, E08, E09, E11, E12, E13, E14, E15, E18, E19, E21, E24, E25, E26, E27, E30, E31, E33, E36	E1, E5a, E5b, E5, E6
QZSS	J01, J02, J03, J07	L1, L2, L5

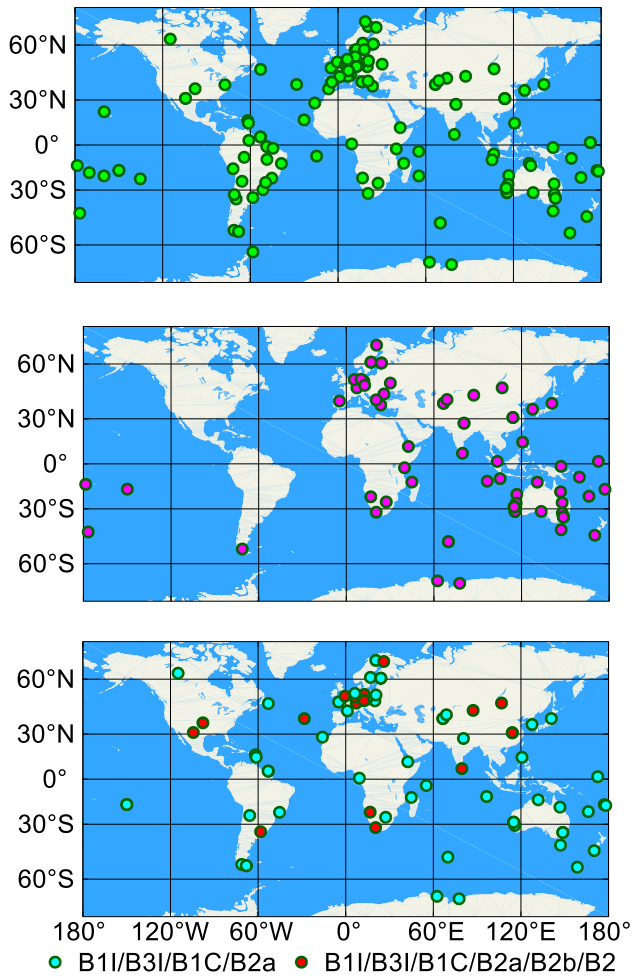

Fig. 1 Distribution of the selected 144 MGEX stations (top), of which 70 stations (middle) can track the BDS-2 signals and 74 stations (bottom) can track the BDS-3 signals

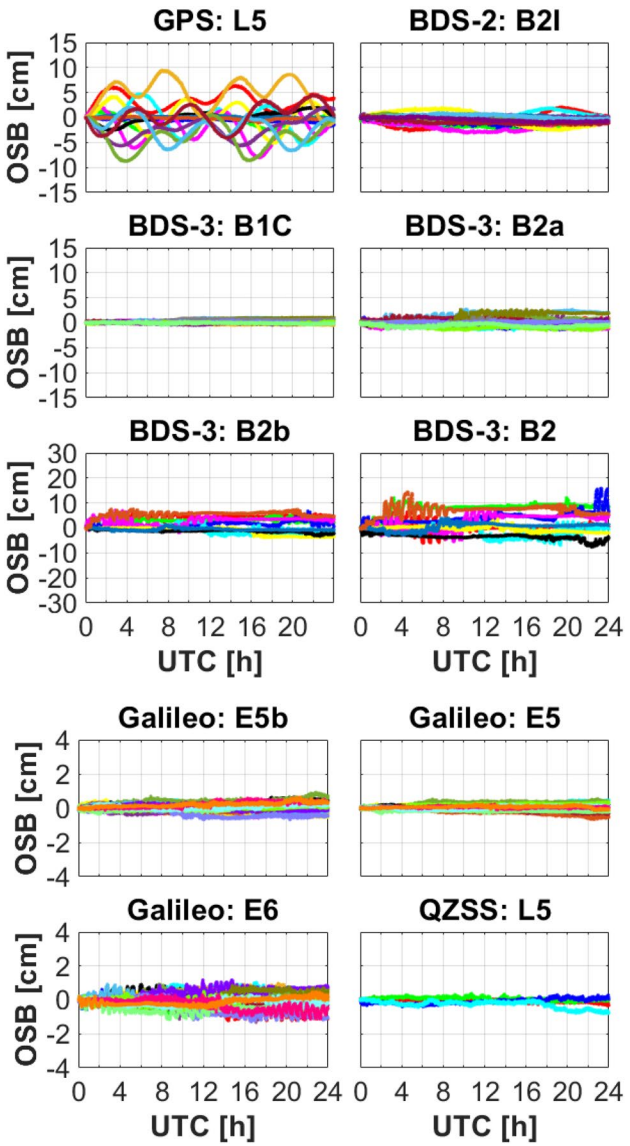

Fig. 2 Carrier phase time-variant OSB time series of the GPS L5, BDS-2 B2I, BDS-3 B1C, B2a, B2b and B2 (top), Galileo E5b, E5, E6 and QZSS L5 (bottom) signals on DOY 288, 2020

QF1, QF2 and QF3 and BDS-3 B1I/B2b/B3I/B2a/B2 FF1, FF2 and FF3 solutions. The positioning errors are modeled as the white noise in kinematic PPP mode. The satellite orbit and clock are fixed by Deutsches GeoForschungsZentrum (GFZ) precise orbit and clock products. The pseudorange observation is corrected with the pseudorange OSB value (Wang et al. 2020). The processing strategies of other error items can refer to the Su and Jin (2020).

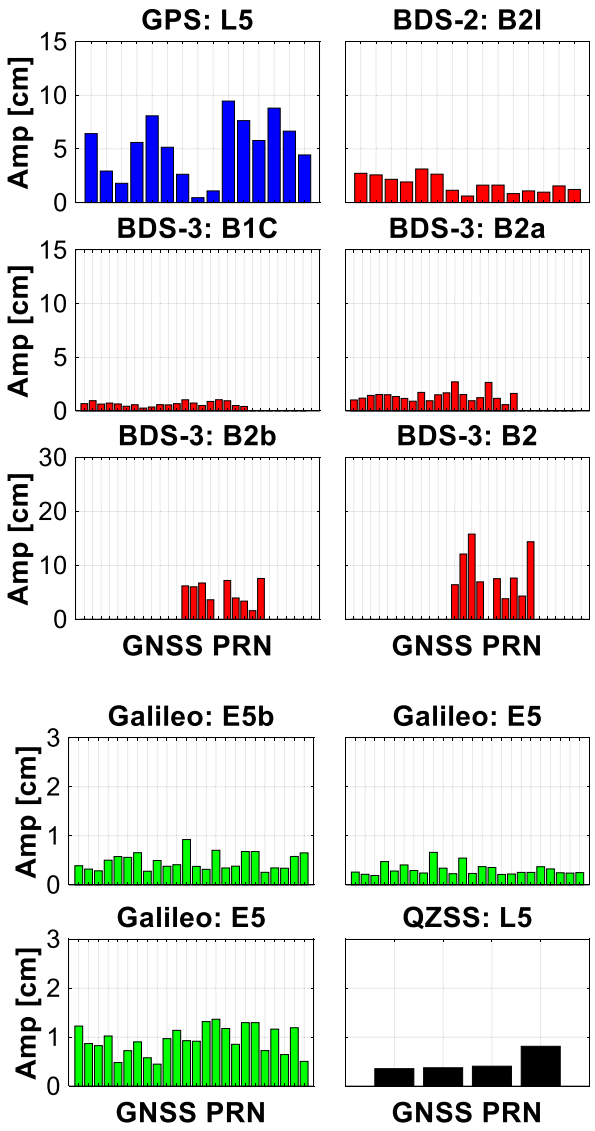

Fig. 3 Amplitudes of the carrier phase time-variant OSB with respect to the GPS L5, BDS-2 B2I, BDS-3 B1C, B2a, B2b and B2 (top), Galileo E5b, E5, E6 and QZSS L5 (bottom) signals on DOY 288, 2020

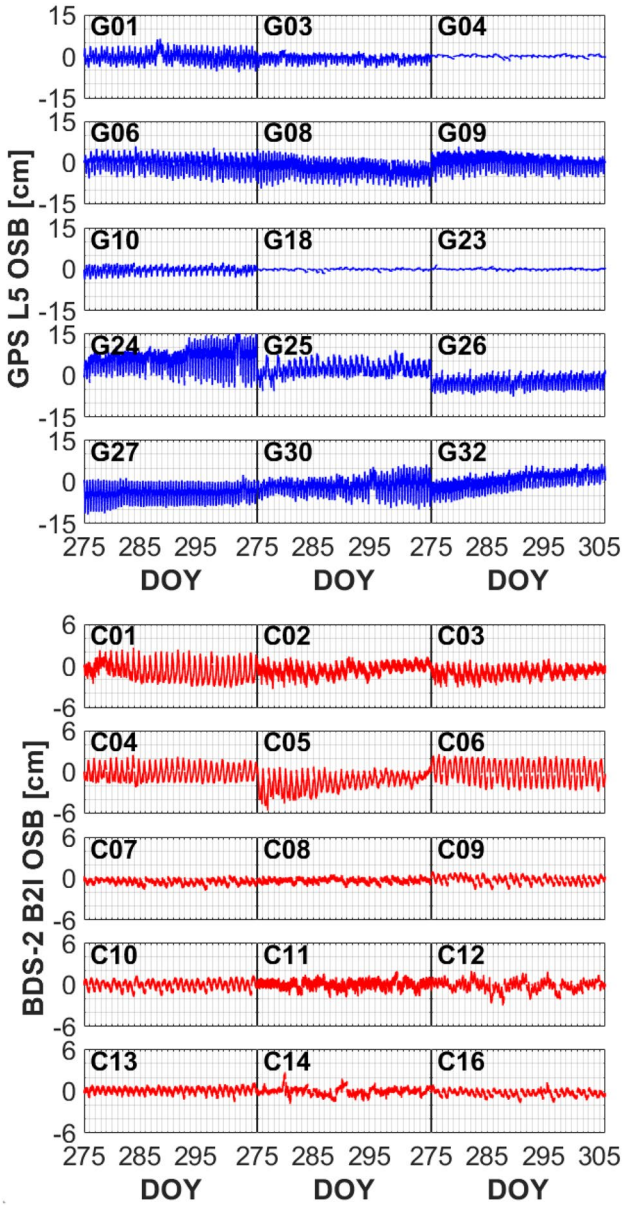

Fig. 4 Time series of the carrier phase time-variant OSB for GPS L5 (top) and BDS-2 B2I (bottom) signals on October 2020

Carrier phase time-variant OSB characteristic and effect on the PPP

The section validates the characteristic of the GNSS carrier phase time-variant OSB. Moreover, the effect of the carrier phase time-variant OSB on GPS/BDS multi-frequency PPP performance is analyzed.

Characteristic of the GNSS carrier phase time-variant OSB

We validate the GNSS carrier phase time-variant OSB characteristic for various GNSS signals, which is estimated with the interval of 30 s. Figure 2 depicts the carrier phase time-variant OSB time series of the GPS L5, BDS-2 B2I, BDS-3 B1C, B2a, B2b and B2, Galileo E5b, E5, E6 and QZSS L5 signals on DOY 288, 2020. Correspondingly, Fig. 3 shows the corresponding carrier phase time-variant OSB amplitudes at each frequency. The satellites whose average observed number in a day is less than 10 are not shown here for the value is not reliable (Li et al. 2013). We can find that the GPS, BDS-2 and BDS-3 signals have the obviously carrier phase time-variant OSB amplitudes, whereas the OSB amplitudes of the Galileo and QZSS are relatively smaller. The carrier phase time-variant OSB amplitude of the GPS L5 signal is in decimeter level, and

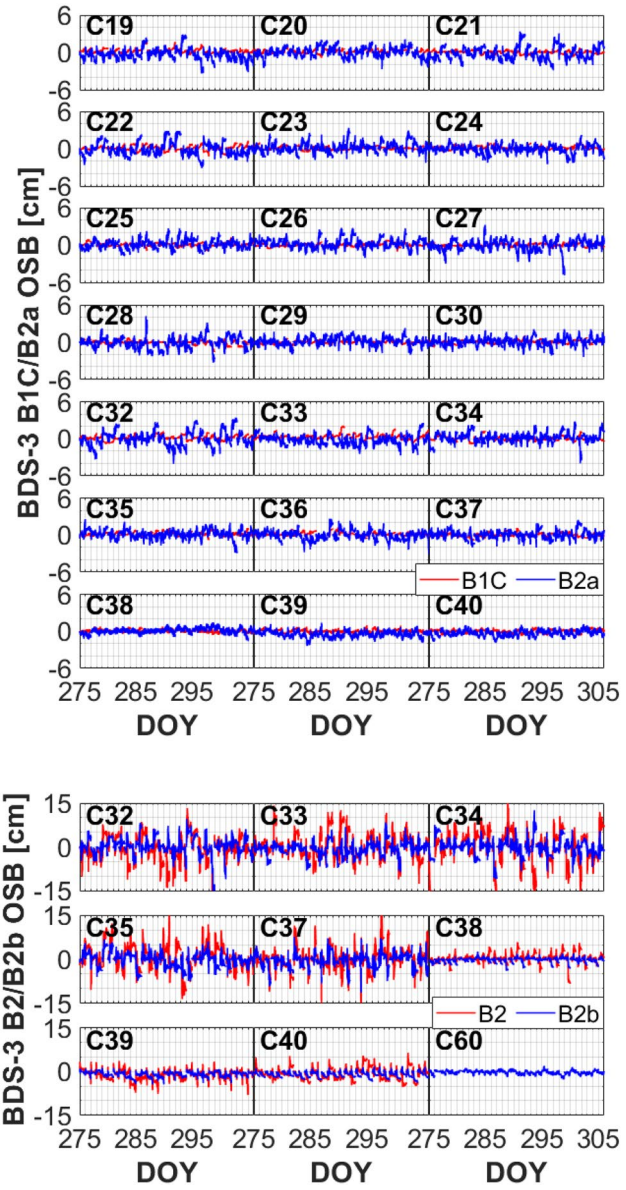

Fig. 5 Time series of the carrier phase time-variant OSB for the BDS-3 B1C, B2a (top), B2 and B2b (bottom) signals on October 2020

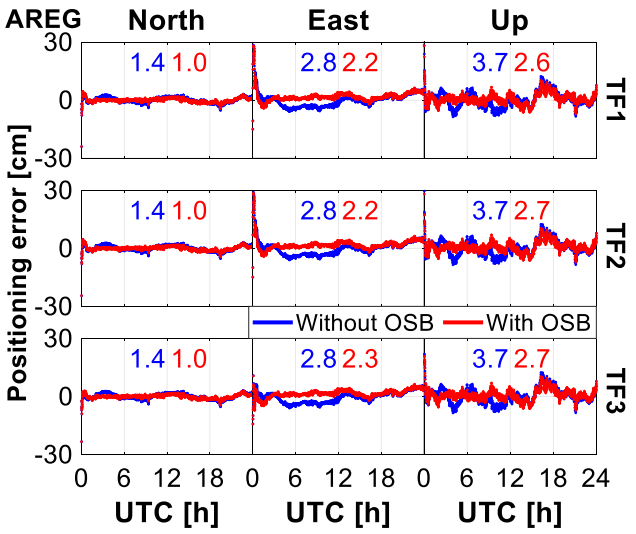

Fig. 6 Positioning error of the GPS-only kinematic L1 + L2 + L5 triple-frequency PPP models on station AREG on DOY 286, 2020

the OSB amplitudes of the BDS-2 B2I, BDS-3 B1C and B2a signals are in the centimeter level. It should be noted that relatively fewer MGEX stations can observe the BDS-3 B2b and B2 signals, and therefore, the corresponding OSB amplitudes are larger and the OSB time series are not stable. Furthermore, the carrier phase time-variant OSB amplitudes of the Galileo E5b and E5 signals are generally less than 1 cm and the Galileo E6 signal amplitude is less than 2 cm. Considering that the single-epoch variation of the carrier phase time-variant OSB is less than 2 mm, we can ignore the effect of the Galileo and QZSS carrier phase time-variant OSB in multi-frequency PPP (Li et al. 2020a). Thereafter, we only concentrate on the GPS and BDS (BDS-2 and BDS-3) carrier phase time-variant OSB and analyze its effect on multi-frequency PPP.

Figures 4 and 5 depict the time series of GPS L5, BDS-2 B2I, BDS-3 B1C, B2a, B2 and B2b signals carrier phase time-variant OSB on October 2020. We can see that the GNSS carrier phase time-variant OSB time series on each day vary with time and the OSB amplitude appears as the periodic signal. The peak-to-peak amplitudes of the single-day GPS L5 carrier phase time-variant OSB for G24 are approximately 15 cm, while the smallest values for G18 and G23 are about 2 cm. According to Montenbruck et al. (2012b), the carrier phase time-variant OSB amplitude is related to the elevation of the sun with respect to the satellite orbital phase. When the absolute value of the sun elevation is larger than 14°, the carrier phase time-variant OSB amplitude will be smaller. Otherwise, the OSB amplitudes will increase to more than a factor of ten. For the BDS-2 B2I carrier phase time-variant OSB, the geosynchronous orbit (GEO) (C01, C02, C03, C04 and C05) and the oldest inclined geosynchronous orbit (IGSO, C06) spacecrafts have the obvious amplitudes, in which the maximum values are approximately 3 cm. The carrier phase time-variant OSB amplitudes of other BDS-2 satellites are nearly confined within 2 cm. The notable periodicity law also exists in the BDS-2 B2I carrier phase time-variant OSB time series. Some carrier phase time-variant OSB values of the BDS-3 satellites are not shown in the figure for their observed satellites are not enough, and the corresponding time series are unreliable. The BDS-3 B2a carrier phase time-variant OSB values have larger amplitudes and poorer stability than the B1C signals with respect to the C19-C40 satellites. Moreover, the BDS-3 B2b and B2 carrier phase time-variant

OSB values exhibit even larger amplitudes and noise levels. Because the number of the MGEX stations tracking the corresponding BDS-3 signals is small, the accuracy and reliability of the carrier phase time-variant OSB estimates are poor, which can be easily affected by the receiver antenna environment, receiver, and antenna quality. It is expected that the carrier phase time-variant OSB of the BDS-3 signals will exhibit better stability with more updated stations capable of tracking the BDS-3 signals. In the practical application, when the average observed number of the stations tracking the satellites is less than 10 in a day, we assume that the corresponding carrier phase time-variant OSB estimates are not applicable in the multi-frequency PPP.

Effect of the GNSS carrier phase time-variant OSB on multi-frequency PPP

To evaluate the effect of the carrier phase time-variant OSB on multi-frequency PPP, we carry out various multi-frequency PPP solutions, including the GPS dual-frequency, BDS-2 dual- and triple-frequency, BDS-3 dual-, triple-, quad- and five-frequency PPP.

GPS multi-frequency PPP

The 24-h observation data for 144 selected stations in a month are used to evaluate the GPS multi-frequency PPP performance. The GPS-only TF1, TF2, and TF3 kinematic PPP solutions are conducted without and with the carrier phase time-variant OSB correction. The dual-frequency L1 + L5 PPP solutions are excluded for the numbers of the observed GPS satellites tracking the L1 and L5 signals in some epochs are less than 4. Figure 6 depicts the positioning error of the GPS-only triple-frequency PPP models on station AREG on DOY 286, 2020. The root mean square (RMS) of the positioning error of the kinematic PPP is also shown. The result indicates that the positioning accuracy of the GPS-only kinematic multi-frequency PPP is significantly improved with the carrier phase time-variant OSB correction. For instance, the GPS-only TF1 PPP exhibits the positioning accuracy of 1.0 cm, 2.2 cm and 2.6 cm in the north, east and up components when correcting the carrier phase time-variant OSB, whereas the positioning accuracy of the case without the carrier phase time-variant OSB correction is 1.4 cm, 2.8 cm and 3.7 cm in three directions, respectively. Figure 7 shows the carrier phase residuals for the GPS-only triple-frequency PPP models on station AREG, in which

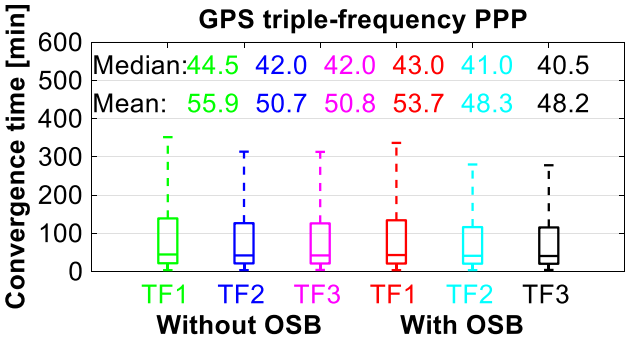

Fig. 8 Boxplot of the convergence time for GPS-only kinematic L1 + L2 + L5 triple-frequency PPP models

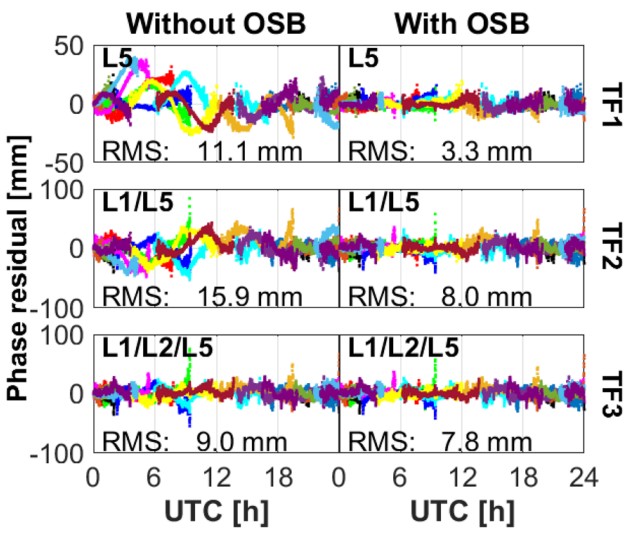

Fig. 7 Carrier phase residuals for the GPS-only kinematic L1 + L2 + L5 triple-frequency PPP models on station AREG on DOY 286, 2020

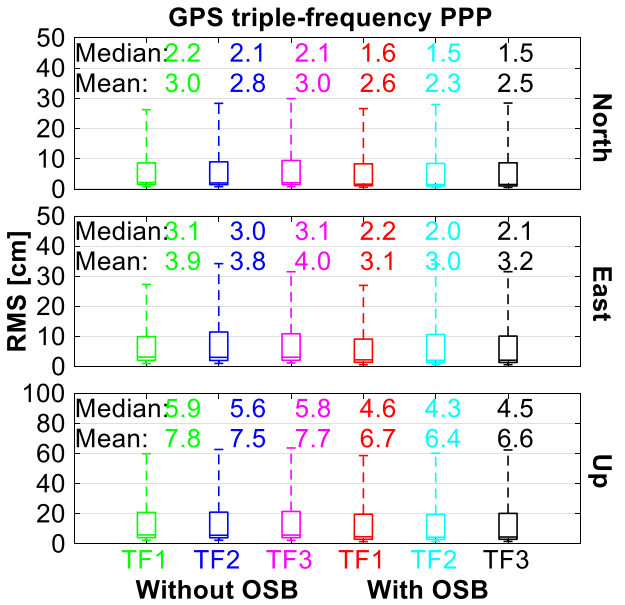

Fig. 9 Boxplot of the positioning accuracy for GPS-only kinematic L1 + L2 + L5 triple-frequency PPP models

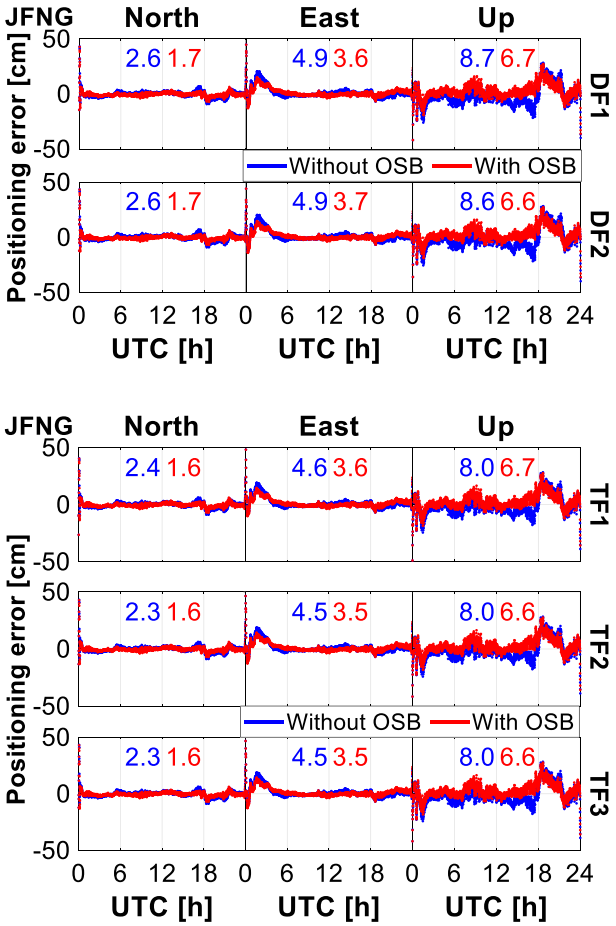

Fig. 10 Positioning error of the BDS-2-only kinematic B1I+B2I dual- (top) and B1I+B2I+B3I triple- (bottom) frequency PPP models on station JFNG on DOY 279, 2020

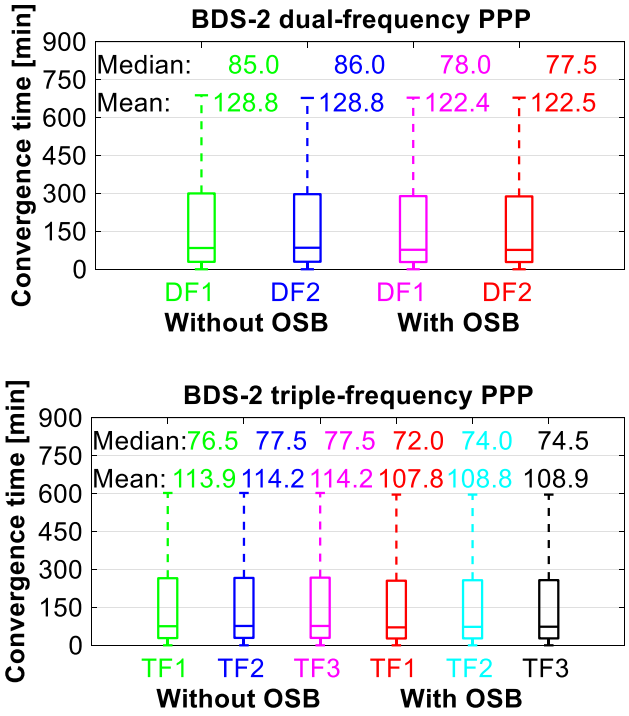

Fig. 11 Boxplot of the convergence time for BDS-2-only kinematic B1I+B2I dual- (top) and B1I+B2I+B3I triple- (bottom) frequency PPP models

different colors identify different satellites. The carrier phase residuals, including the measurement and unmodeled noises, are analyzed for the 24-h result. The RMS values of the residuals for the L5, L1+L5 and L1+L2+L5 combined measurements are different owing to the different noise amplification factors. Systematic errors can be observed for the GPS-only triple-frequency PPP solutions without the carrier phase time-variant OSB correction. After applying the correction, the RMS of the carrier phase residuals is obviously reduced. The RMS values of the carrier phase observation residuals reduce from 11.1 mm, 15.9 mm and 9.0 mm to 3.3 mm, 8.0 mm and 7.8 mm with the carrier phase time-variant OSB correction for the GPS TF1, TF2 and TF3 PPP solutions, respectively.

Figure 8 depicts the boxplot of the convergence time of the GPS-only kinematic triple-frequency PPP models. Moreover, Fig. 9 elucidates the boxplot of the positioning accuracy for GPS-only kinematic triple-frequency PPP models in the north, east and up components. The corresponding median and mean values are also depicted in the figures. The convergence epoch is defined as the positioning errors kept within 10 cm from the current epoch to the next 20 epochs. We can see that the GPS-only kinematic PPP positioning performance in terms of the convergence time and positioning accuracy is significantly improved with the GPS carrier phase time-variant OSB correction. For instance, the GPS-only kinematic PPP mean convergence time of the TF1, TF2 and TF3 models is reduced from 55.9 min, 50.7 min and 50.8 min to 53.7 min, 48.3 min and 48.2 min, respectively. The GPS-only kinematic TF1 PPP model without the carrier phase time-variant OSB correction can exhibit the positioning accuracy of 3.0 cm, 3.9 cm and 7.8 cm in the north, east and up components, respectively, while the corresponding positioning accuracy can be improved to 2.6 cm, 3.1 cm and 6.7 cm in three components with the carrier phase time-variant OSB correction. The different GPS-only kinematic triple-frequency PPP models exhibit the nearly same positioning accuracy after convergence following the equivalence principle (Su and Jin 2020).

BDS-2 multi-frequency PPP

BDS-2 satellites can transmit the B1I, B2I and B3I triple-frequency signals. The GFZ analysis center has two parallel product lines with long and short file names. The BDS-3 and BDS-2 satellites are processed together using the B1I/

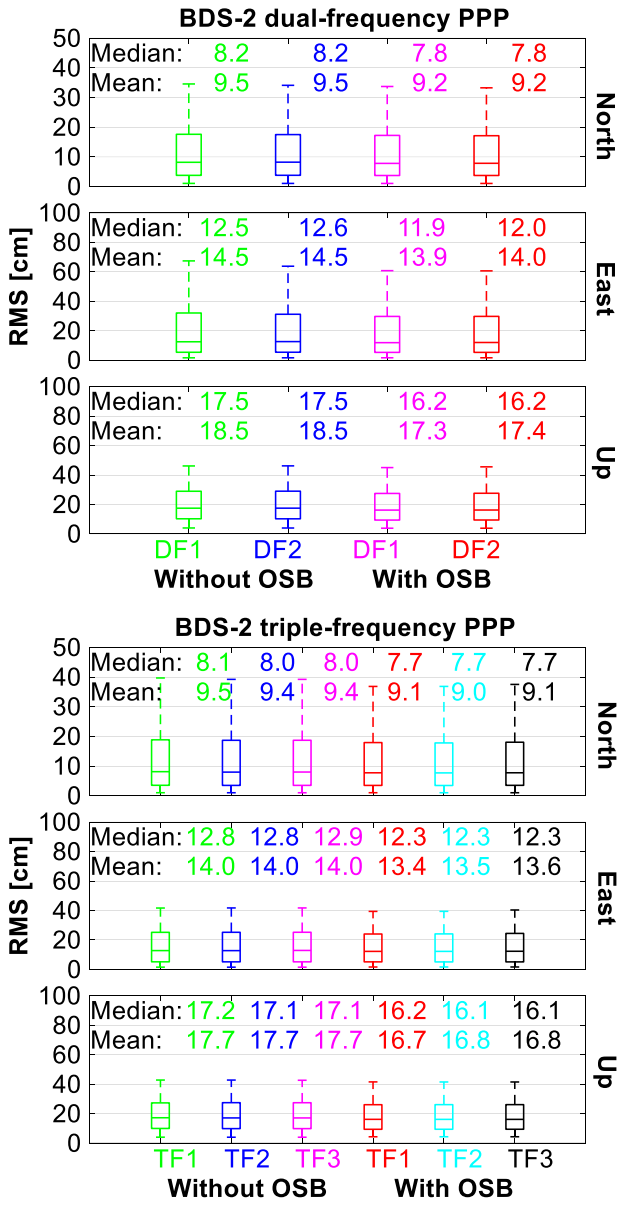

Fig. 12 Boxplot of the positioning accuracy for BDS-2-only kinematic B1I + B2I dual- (top) and B1I + B2I + B3I triple- (bottom) frequency PPP models

B3I observations in the long file name product. The BDS-2 satellites are only handled using the B1I/B2I observations in the short name product (ftp://ftp.gfz-potsdam.de/pub/GNSS/products/mgex/README.txt). Owing to the applied BDS-2 satellite clock product is based on the satellite PCE using the IF B1I/B3I observations, the B2I observations need the correction of carrier phase time-variant OSB. Hence, the dual-frequency B1I + B2I and triple-frequency B1I + B2I + B3I BDS-2 PPP solutions are conducted. 70 stations that can observe enough BDS-2 satellites in Fig. 1 are selected to conduct the BDS-2 multi-frequency PPP. Figure 10 depicts the positioning error of the BDS-2 triple-frequency PPP models on station JFNG on DOY 279, 2020. The result indicates that the triple-frequency PPP positioning performance is slightly better than dual-frequency solutions. With the BDS-2 B2I carrier phase time-variant OSB correction, the dual- and triple-frequency kinematic PPP positioning accuracy is significantly improved for the station JFNG. For example, the BDS-2 only kinematic TF1 PPP model exhibits the positioning accuracy of 1.6 cm, 3.6 cm and 6.7 cm in the north, east and up components with the carrier phase time-variant OSB correction, while the positioning accuracy is 2.4 cm, 4.6 cm and 8.0 cm without the correction.

Figure 11 depicts the boxplot of the convergence time for BDS-2-only kinematic dual- and triple-frequency PPP models. Figure 12 shows the boxplot of the positioning accuracy for BDS-2-only kinematic dual- and triple-frequency PPP models without and with the carrier phase time-variant OSB correction in the north, east and up components. The BDS-2-only triple-frequency PPP models exhibit better performance than the dual-frequency solutions. Moreover, the BDS-2-only kinematic PPP performance can improve the positioning performance with the carrier phase time-variant OSB correction. For instance, the mean convergence time of the DF1, DF2, TF1, TF2 and TF3 BDS-2-only kinematic PPP models is reduced by 5.0%, 4.9%, 5.4%, 4.7% and 4.6%, respectively, with the carrier phase time-variant OSB correction. The mean RMS values of the positioning errors for the five PPP models with the carrier phase time-variant OSB correction are (9.2, 13.9, 17.3) cm, (9.2, 14.0, 17.4) cm, (9.1, 13.4, 16.7) cm, (9.0, 13.5, 16.8) cm, and (9.1, 13.6, 16.8) cm in the north, east and up components, respectively.

BDS-3 multi-frequency PPP

The newly BDS-3 satellites can broadcast more signals including the B1I, B3I, B1C, B2a, B2b and B2 signals. For the 144 selected stations, 74 stations can synchronously observe the B1I/B3I/B1C/B2a signals and 20 stations are able to track all the B1I/B3I/B1C/B2a/B2b/B2 signals. To analyze the effect of the carrier phase time-variant OSB on BDS-3 multi-frequency PPP solutions, we carried out various BDS-3-only kinematic multi-frequency PPP solutions, including the B1C + B2a dual-frequency, B1I + B3I + B2a triple-frequency, B1I + B3I + B1C + B2a quad-frequency and B1I + B3I + B2b + B2a + B2 five-frequency PPP solutions. Figure 13 depicts the positioning error of the BDS-3-only kinematic dual-, triple-, quad- and five-frequency PPP models on station SUTM on DOY 282, 2020. Only a fraction of carrier phase time-variant OSB values estimated with enough sites are stable and useable. Thereby, the improvement of the carrier phase time-variant OSB on BDS-3 multi-frequency PPP solutions is weak. The positioning accuracy of the BDS-3-only kinematic PPP for the B1C + B2a

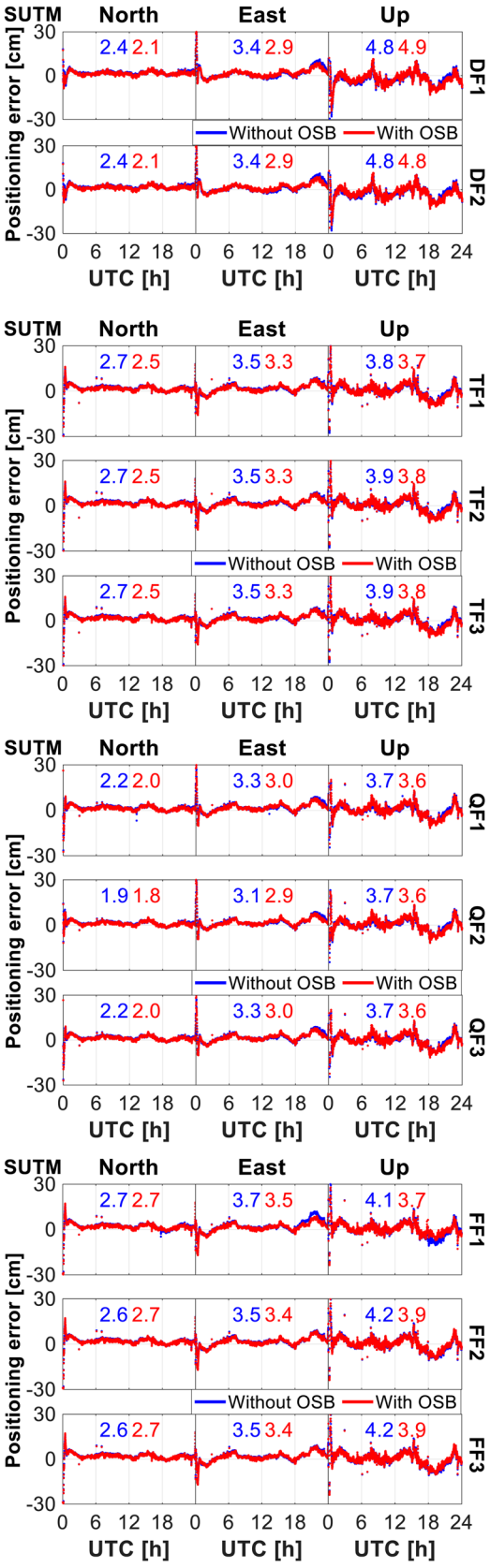

Fig. 13 Positioning error of the BDS-3-only kinematic B1C + B2a dual-, B1I + B3I + B2a triple-, B1I + B3I + B1C + B2a quad- and B1I + B3I + B2b + B2a + B2 five-frequency PPP models on station SUTM on DOY 282, 2020

DF1, B1I + B3I + B2a TF1, B1I + B3I + B1C + B2a QF1, B1I + B2b + B3I + B2a + B2 FF1 solutions with the carrier phase time-variant OSB correction is (2.1, 2.9, 4.9) cm, (2.5, 3.3, 3.7) cm, (2.0, 3.0, 3.6) cm, and (2.7, 3.5, 3.7) cm, respectively, in the north, east and up directions. Spikes can be seen in the BDS-3 multi-frequency PPP solutions in some epochs for positioning performance is affected by the observation quality. The five-frequency PPP solutions do not exhibit the best positioning performance, for they apply the observation on different frequencies, which do not conflict with the point of view that the positioning performance can be improved with more observations.

Figure 14 elucidates the convergence time for BDS-3-only kinematic dual-, triple-, quad- and five-frequency PPP models. Figure 15 illuminates the positioning accuracy for BDS-3-only kinematic dual-, triple-, quad- and five-frequency PPP models. The reduction of convergence time of the BDS-3-only kinematic multi-frequency PPP with the carrier phase time-variant OSB correction is at the level of a few minutes. The mean convergence time of the BDS-3-only kinematic DF1, DF2, TF1, TF2, TF3, QF1, QF2, QF3, FF1, FF2 and FF3 solutions with the carrier phase time-variant OSB correction is 100.5, 100.7, 97.3, 97.6, 97.6, 92.9, 97.3, 94.8, 97.2, 96.6, and 96.5 min, respectively. With the carrier phase time-variant OSB correction, the positioning accuracy of the BDS-3-only kinematic multi-frequency PPP is improved but not obvious. Compared to the BDS-3 dual-frequency PPP, the multi-frequency PPP positioning performance in terms of the positioning accuracy and convergence time is slightly improved.

Conclusion

The disagreement of the precise satellite clock estimated by different observations is known as the IFCB. To overcome the inconsistency of the carrier phase biases, the definition of the carrier phase time-variant OSB is present. The advantage of the carrier phase time-variant OSB is that it can be directly applied on the homologous carrier phase observations, and thus, the effect of the carrier phase IFCB can be eliminated. 144 MGEX stations are used to estimate the GNSS carrier phase time-variant OSB and analyze its effect on the GNSS multi-frequency PPP solutions.

The GPS, BDS-2 and BDS-3 carrier phase time-variant OSB time series have the obvious amplitudes, but the amplitudes of the Galileo and QZSS OSB are small. Hence, the Galileo and QZSS carrier phase time-variant OSB effect

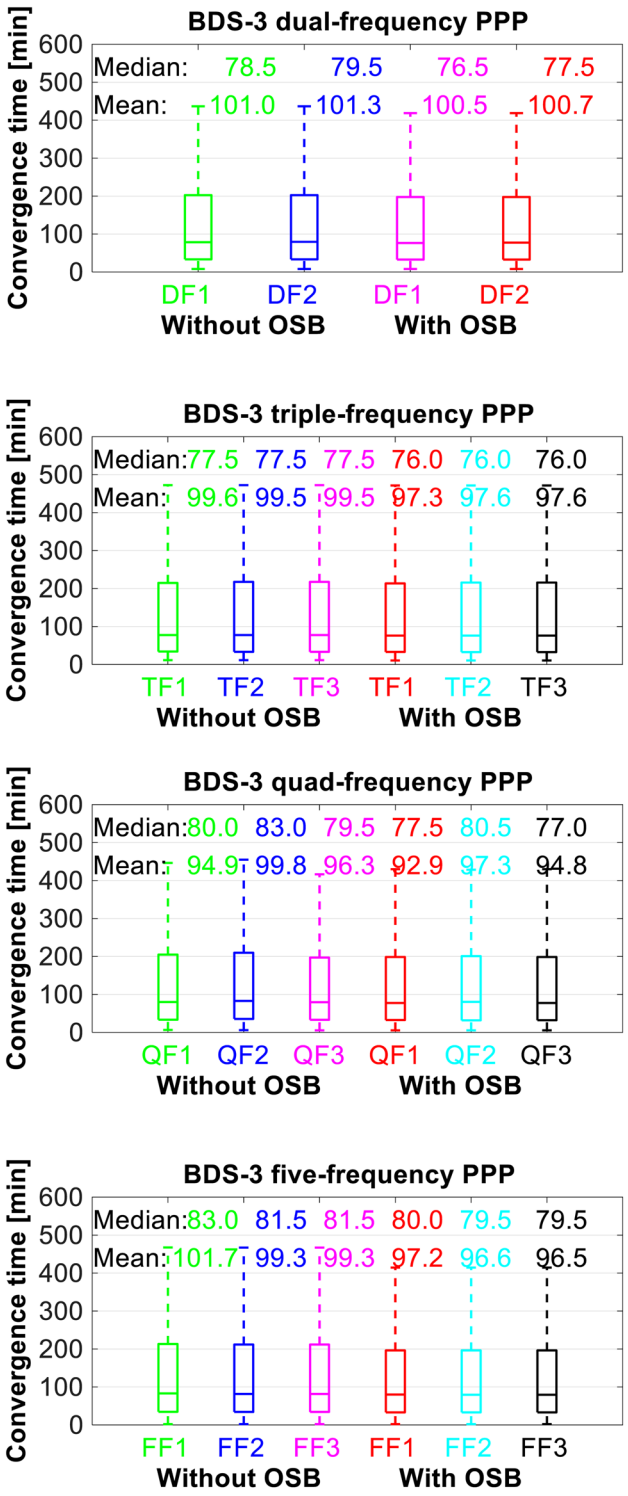

Fig. 14 Boxplot of the convergence time for BDS-3-only kinematic B1C + B2a dual-, B1I + B3I + B2a triple-, B1I + B3I + B1C + B2a quad- and B1I + B3I + B2b + B2a + B2 five-frequency PPP models

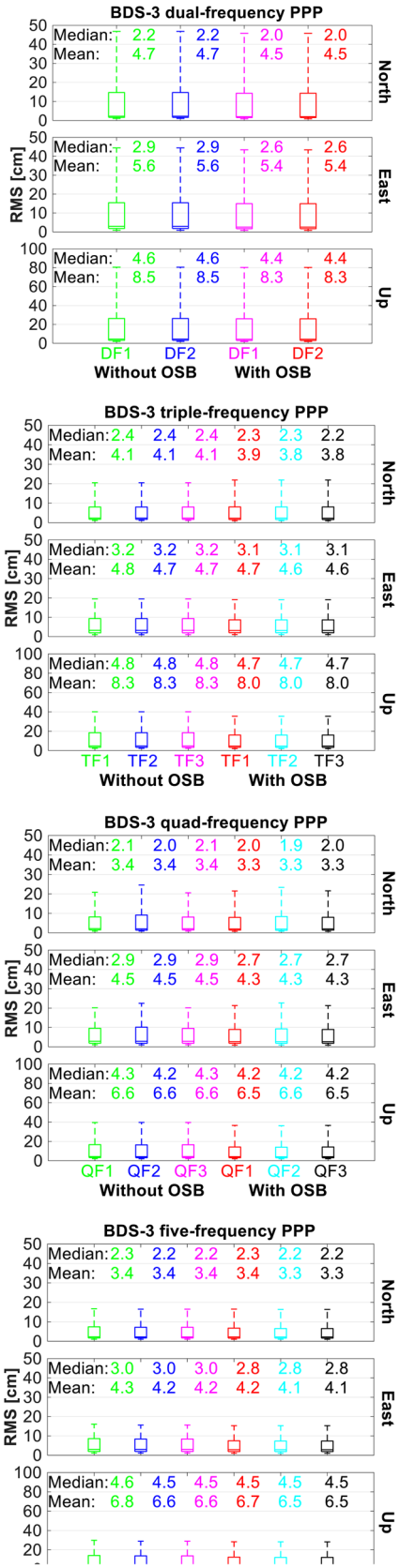

Fig. 15 Boxplot of the positioning accuracy for BDS-3-only kinematic B1C + B2a dual-, B1I + B3I + B2a triple-, B1I + B3I + B1C + B2a quad- and B1I + B3I + B2b + B2a + B2 five-frequency PPP models

in multi-frequency PPP can be neglected. With the carrier phase time-variant OSB correction, the GPS and BDS-2 multi-frequency positioning performance is improved obviously, whereas the improvement of the BDS-3 multi-frequency PPP solutions is weak. The reason is that the accuracy of the carrier phase time-variant OSB estimated with relatively fewer stations is low. With the carrier phase time-variant OSB correction, the mean convergence time of GPS-only kinematic PPP can reduce several minutes, and the positioning accuracy can improve at the centimeter level. The BDS-2-only kinematic dual- and triple-frequency PPP can also exhibit the better convergence speed with the carrier phase time-variant OSB correction, and the improvement of the positioning accuracy is in the millimeter level. The GNSS carrier phase time-variant OSB concept is demonstrated that it is reasonable and beneficial for the GNSS community.

Acknowledgements We appreciate the reviewers and editors' valuable comment to improve the paper quality.

Data availability The used GNSS observation data are provided by the MGEX network (ftp://igs.ign.fr/pub/igs/data/campaign/mgex/daily/rinex3/). The precise products are provided by the GFZ (ftp://ftp.gfz-potsdam.de/GNSS/products/mgex/).

References

Cai C, He C, Santerre R, Pan L, Cui X, Zhu J (2016) A comparative analysis of measurement noise and multipath for four constellations: GPS, BeiDou, GLONASS and Galileo. Surv Rev 48:287–295

Dvulit P, Savchuk S, Sosonka I (2021) Accuracy estimation of site coordinates derived from GNSS-observations by non-classical error theory of measurements. Geod Geodyn 12(5):347–355

Erol S, Alkan R, Ozulu İ, İlçi V (2020) Performance analysis of real-time and post-mission kinematic precise point positioning in marine environments. Geod Geodyn 11(6):401–410

Guo J, Geng J (2018) GPS satellite clock determination in case of inter-frequency clock biases for triple-frequency precise point positioning. J Geod 92:1133–1142

Hauschild A, Steigenberger P, Rodriguez-Solano C (2012) Signal, orbit and attitude analysis of Japan's first QZSS satellite Michibiki. GPS Solut 16:127–133

Khodabandeh A, Teunissen P (2016) PPP-RTK and inter-system biases: the ISB look-up table as a means to support multi-system PPP-RTK. J Geod 90:837–851

Leick A, Rapoport L, Tatarnikov D (2015) GPS satellite surveying. Wiley, Hoboken

Li H, Zhou X, Wu B, Wang J (2012) Estimation of the inter-frequency clock bias for the satellites of PRN25 and PRN01 Science China Physics. Mech Astron 55:2186–2193

Li H, Zhou X, Wu B (2013) Fast estimation and analysis of the inter-frequency clock bias for Block IIF satellites. GPS Solut 17:347–355

Li H, Li B, Xiao G, Wang J, Xu T (2016) Improved method for estimating the inter-frequency satellite clock bias of triple-frequency GPS. GPS Solut 20:751–760

Li P, Jiang X, Zhang X, Ge M, Schuh H (2020a) GPS+ Galileo+ BeiDou precise point positioning with triple-frequency ambiguity resolution. GPS Solut 24:1–13

Li X, Liu G, Li X, Zhou F, Feng G, Yuan Y, Zhang K (2020b) Galileo PPP rapid ambiguity resolution with five-frequency observations. GPS Solut 24:1–13

Liu T, Zhang B, Yuan Y, Zhang X (2020) On the application of the raw-observation-based PPP to global ionosphere VTEC modeling: an advantage demonstration in the multi-frequency and multi-GNSS context. J Geod 94:1–20

Ma X, Yu K, Wang E, He X, Lu T, Li Q (2021) Evaluation of BDS and GPS RAIM availability based on data collected in June 2020. Geod Geodyn 12(3):181–189

Montenbruck O, Hugentobler U, Dach R, Steigenberger P, Hauschild A (2012a) Apparent clock variations of the Block IIF-1 (SVN62) GPS satellite. GPS Solut 16:303–313

Montenbruck O, Hugentobler U, Dach R, Steigenberger P, Hauschild A (2012b) Apparent clock variations of the Block IIF-1 (SVN62) GPS satellite. GPS Solut 16:303–313

Odijk D, Zhang B, Khodabandeh A, Odolinski R, Teunissen PJ (2016) On the estimability of parameters in undifferenced, uncombined GN network and PPP-RTK user models by means of S-system theory. J Geod 90:15–44

Pan L, Li X, Zhang X, Li X, Lu C, Zhao Q, Liu J (2017a) Considering inter-frequency clock bias for BDS triple-frequency precise point positioning. Remote Sens 9:734

Pan L, Zhang X, Li X, Liu J, Li X (2017b) Characteristics of inter-frequency clock bias for Block IIF satellites and its effect on triple-frequency GPS precise point positioning. GPS Solut 21:811–822

Pan L, Zhang X, Guo F, Liu J (2019) GPS inter-frequency clock bias estimation for both uncombined and ionospheric-free combined triple-frequency precise point positioning. J Geod 93:473–487

Schaer S (2016) SINEX BIAS—solution (Software/technique) INdependent EXchange Format for GNSS BIASes Version 1.00. In: IGS workshop on GNSS biases, Bern, Switzerland

Su K, Jin S (2020) Analysis and comparisons of the BDS/Galileo quad-frequency PPP models performances. Acta Geod Cartogr Sin 49:1189

Su K, Jin S (2021) Analytical performance and validations of the Galileo five-frequency precise point positioning models. Measurement 172:108890

Wang N, Yuan Y, Li Z, Montenbruck O, Tan B (2016) Determination of differential code biases with multi-GNSS observations. J Geod 90:209–228

Wang N, Li Z, Duan B, Hugentobler U, Wang L (2020) GPS and GLONASS observable-specific code bias estimation: comparison of solutions from the IGS and MGEX networks. J Geod 94:1–15

Wanninger L, Sumaya H, Beer S (2017) Group delay variations of GPS transmitting and receiving antennas. J Geod 91:1099–1116

Zhang B, Chen Y, Yuan Y (2019) PPP-RTK based on undifferenced and uncombined observations: theoretical and practical aspects. J Geod 93:1011–1024

Zhang B, Teunissen P, Yuan Y (2017) On the short-term temporal variations of GNSS receiver differential phase biases. J Geod 1–10

Zhao Q, Wang C, Guo J, Wang B, Liu J (2018) Precise orbit and clock determination for BeiDou-3 experimental satellites with yaw attitude analysis. GPS Solut 22:1–13

Ke Su received his doctoral degree at the University of Chinese Academy of Sciences, Beijing, China. His research interests include GNSS PPP and ionosphere applications.

Shuanggen Jin is a Professor at the Shanghai Astronomical Observatory. His main research areas include Satellite Navigation, Space Geodesy, Remote Sensing, Climate Change and Space/Planetary Exploration.

Guoqiang Jiao is currently a doctoral degree candidate at the Shanghai Astronomical Observatory, Chinese Academy of Sciences, Shanghai, China. His main research interests are PCE and its applications.